Mechanotransduction by Pcdh15 relies on a novel *cis*-dimeric architecture

Gilman Dionne[1,2], Xufeng Qiu[3], Micah Rapp[1,2,4], Xiaoping Liang[3], Bo Zhao[3], Guihong Peng[3], Phinikoula S. Katsamba[1,2,5], Goran Ahlsen[1,2,5], Rotem Rubinstein[1,5,6], Clinton S. Potter[1,4], Bridget Carragher[1,4], Barry Honig[1,2,5,6*], Ulrich Müller[3*], and Lawrence Shapiro[1,2,6*†]

[1]Department of Biochemistry and Molecular Biophysics, [2]Zuckerman Mind Brain, [5]Howard Hughes Medical Institute, [6]Departments of Systems Biology and Medicine, Columbia University, New York, NY 10032, USA.

[3]The Solomon H. Snyder Department of Neuroscience, Johns Hopkins University School of Medicine, Baltimore, MD 21205, USA.

[4]National Resource for Automated Molecular Microscopy, Simons Electron Microscopy Center, New York Structural Biology Center, New York, NY 10027, USA. [*] Correspondence: lss8@columbia.edu (L.S.); umuelle3@jhmi.edu (U.M.); bh6@cumc.columbia.edu (B.H.)

[†]Lead contact

Summary (150 words)

The tip link, a filament formed by protocadherin 15 (Pcdh15) and cadherin 23, conveys mechanical force from sound waves and head movement to open hair-cell mechanotransduction channels. Tip-link cadherins are thought to have acquired structural features critical for their role in mechanotransduction. Here we biophysically and structurally characterize the unusual *cis*-homodimeric architecture of Pcdh15. We show that Pcdh15 molecules form double helical assemblies through *cis*-dimerization interfaces in the extracellular cadherin EC2-EC3 domain region and in a unique membrane-proximal domain. Electron microscopy studies visualize the *cis*-dimeric Pcdh15 assembly and reveal the Pcdh15 extracellular domain as a parallel double-helix with *cis* cross-bridges at the two locations we defined. The helical configuration suggests the potential for elasticity through helix winding/unwinding. Functional studies in hair cells show that mutations that perturb Pcdh15 dimerization contacts affect mechanotransduction. Together, these data reveal the *cis*-dimeric architecture of Pcdh15, and show that dimerization is critical for sensing mechanical stimuli.

Introduction

Mechanosensitive hair cells use a bundle of stereocilia at their apical surface to detect mechanical stimuli evoked by sound (acoustic) or motion (vestibular) and transduce them into electrical signals, a process termed mechanoelectrical transduction (MET) (Hudspeth, 2014; Pan and Holt, 2015; Pepermans and Petit, 2015; Ricci et al., 2006; Zhao and Muller, 2015) (Figure 1A). Rows of stereocilia in hair bundles are arranged by height; deflections from the shortest toward the tallest stereocilia leads to the opening of mechanically gated ion channels near the tips of stereocilia (Assad et al., 1991; Hudspeth, 2014; Hudspeth and Jacobs, 1979). These ion channel are located near a ~200 nm long protein tether – the tip link – which couples the tip of one stereocilium to a more apical location on the side of a taller stereocilium (Figure 1B) (Pickles et al. 1984; Assad et al. 1991; Kachar et al. 2000; Kazmierczak et al. 2007; Beurg et al. 2009). Freeze etched EM images obtained in vivo and low-resolution negative stain EM images obtained in vitro suggest that the tip link is a tightly wound helix consisting of two associated strands (Kachar et al., 2000; Kazmierczak et al., 2007). Forces from sound or motion induce deflection of hair bundles, imparting increased tension on the tip link, leading to an increase in the open probability of the mechanically gated ion channels (Hudspeth, 2014). There remains a debate as to whether the tip link functions as the putative gating spring for the opening of the associated mechanotransduction channel (Ricci et al., 2006; Zhao and Muller, 2015).

The tip link is composed of Pcdh15 and Cdh23, both members of the cadherin superfamily. Tip-link cadherins show unusual features, which clearly distinguish them from classical cadherins. First, tip-link cadherins are unusually large. While the extracellular regions of classical cadherins consist of 5 extracellular cadherin (EC) domains, the extracellular regions of Pcdh15 and Cdh23 contain 11 and 27 EC domains, respectively (Ahmed et al., 2006; Ahmed

et al., 2001; Bolz et al., 2001; Kazmierczak et al., 2007; Siemens et al., 2004). Additionally, Pcdh15 has a conserved region of approximately 130 amino acids between EC11 and the transmembrane domain. This region has no homology to any protein of known structure, yet secondary structure prediction algorithms indicate it to be a folded domain. Since this region is localized at the expected site of ion-channel interaction, we refer to this domain as the Protocadherin 15 Interacting-Channel Associated – or PICA – domain. Second, unlike classical cadherins, the extracellular domains of Pcdh15 and Cdh23 are thought to form helical parallel *cis*-homodimers suggesting multiple tight contact points between parallel strands (Kazmierczak et al., 2007). The parallel *cis* homodimer is thought to be the principle functional unit of Pcdh15 and Cdh23 (Ahmed et al., 2006; Kazmierczak et al., 2007; Siemens et al., 2004; Sotomayor et al., 2012). Classical cadherins instead form large lateral clusters consisting of many cadherin monomers (Harrison et al., 2011; Indra et al., 2018; Vester-Christensen et al., 2013) . Finally, the *trans*-dimer interface between Pcdh15 and Cdh23 differs from the interface between classical cadherins. *Trans*-interactions in classical cadherins are mediated by EC1 and critically depend on a conserved tryptophan (Boggon et al., 2002; Shan et al., 1999; Shapiro et al., 1995). In contrast, the EC1 domains of Pcdh15 and Cdh23 lack this conserved tryptophan and the two cadherins instead appear to interact through a "hand-shake" like mode via distinct interfaces in their EC1 and EC2 domains (Elledge et al., 2010; Sotomayor et al., 2010, 2012). Thus, lateral homodimerization, helix formation, and a novel *trans* adhesive dimer interface are specializations of Pcdh15 and Cdh23 that likely evolved for their critical function in mechanotransduction. Crystallographic studies have provided first insights into the structure of monomeric fragments of Pcdh15 (Araya-Secchi et al., 2016; Powers et al., 2017; Sotomayor et

al., 2010, 2012), but we know little about the mechanisms that drive dimerization and helix formation, or that constitute the adhesive interface in the trans tetramer.

Here we have used crystallography, electron microscopy, and solution biophysics to show that *cis* homodimerization of Pcdh15 is mediated by a novel interaction mode not observed previously for other members of the cadherin superfamily. While previous structural studies of Pcdh15 utilized fragments expressed in bacteria, most of which appeared monomeric (Araya-Secchi et al., 2016; Powers et al., 2017; Sotomayor et al., 2012), we focused on proteins expressed in eukaryotic cells thus containing modifications such as glycosylations that might affect protein function. We identified two distinct interfaces that mediate homodimerization in Pcdh15: one near the *trans*-adhesive interface that is contained within domains EC2 and EC3, and the other adjacent to the membrane mediated by the non-cadherin PICA domain. The crystal structure of the *cis*-dimeric EC1-EC3 region of Pcdh15 reported here reveals the structural elements that drive homodimerization in the membrane-distal *cis*-dimer interface. Negative stain single-particle electron microscopy and 3D reconstruction reveal the overall *cis*-dimeric architecture of the Pcdh15 ectodomain. Functional assays provide strong evidence that the molecular interactions that drive *cis*-dimerization of Pcdh15 are critical for sensing mechanical stimuli by hair cells.

RESULTS

Identifying the minimal *cis*-dimeric region of Pcdh15

To investigate the structural basis for Pcdh15 *cis*-homodimerization, we first endeavored to identify fragments from within the Pcdh15 cadherin repeat region that form dimers. Using a mammalian HEK 293-cell expression system, we produced a series of constructs that 'walk' the length of the 11 cadherin domains of the mouse Pcdh-15 ectodomain in two-domain fragments,

and interrogated their dimeric properties via sedimentation equilibrium analytical ultracentrifugation (AUC) (Figure 2, Figure S1, Table S2). Only the EC2-3 and EC3-4 constructs – constructs that both contained EC3 – were dimers in solution. While the EC7-8 construct appeared weakly dimeric (K_D = 208 μM), the value of the isodesmic constant (K_I = 343 μM) indicates that this interaction is nonspecific.

While most two-domain constructs of Pcdh15 could be produced, two constructs, EC8-9 and EC10-11, failed to express. To ensure full coverage of the Pcdh15 ectodomain, and to potentially enhance weak binding affinities of the two-domain fragments, we carried out similar 'domain walking' experiments with both three- and four-domain constructs (Figure 2, Table S2). Although three of these additional thirteen fragments did not express, the combination of 2-, 3-, and 4-domain fragments achieved full coverage of the cadherin repeat region of the Pcdh15 ectodomain. The only four-domain construct that was dimeric was EC3-6, which showed dimerization behavior similar to the other constructs containing EC3. Overall, these data show that Pcdh15 forms a relatively strong *cis*-dimeric interaction that involves the EC3 domain.

Analysis of Pcdh15 sequences from numerous species revealed that the PICA domain succeeding the 11 EC domains and preceding the membrane insertion point was highly conserved (Figure S2). We produced constructs that contained the PICA domain to characterize their *cis*-association state. Although the PICA domain region failed to express in isolation or when preceded by the final EC domain, a construct encoding EC10-EC11-PICA was well behaved. Multi-angle light scattering (MALS) analysis showed that this EC10-EC11-PICA domain construct was also dimeric (Figure S3). The dimeric nature of the EC10-EC11-PICA domain protein, combined with the monomeric nature of fragments lacking the PICA domain but

containing EC10-EC11, suggest that the PICA domain mediates *cis*-dimerization of Pcdh15 near the membrane insertion point.

Crystal structure of an EC1-3 Pcdh15 *cis* homodimer

Since we detected *cis* dimerization in the EC3 region, we produced an EC1-3 construct for structure determination. This construct contained both the *cis*-interacting region and the Cadherin-23-*trans*-interacting region located in EC1-2. Consistent with the AUC results (Figure 2), the Pcdh15 EC1-3 protein acted as a dimer in MALS (Figure S3), with a measured molecular mass of 88 kDa that is about twice the mass of the predicted mass of a monomer (41.7 kDa). Pcdh15 EC1-3 also acted as a dimer in sedimentation equilibrium AUC with a binding affinity of 1.2 μM (Figure S1). We determined the crystal structure of this molecule to 1.7 Å resolution (Figure 3) by molecular replacement using a two-domain structure of Pcdh15 (PDB 4APX) as a search model (Sotomayor et al., 2012). Data and refinement statistics are shown in Table S1.

The Pcdh15 EC1-3 protomers are arranged in a parallel homodimer in which the overall architecture resembles an open pair of scissors with the homodimer interface, centered around the EC2-3 junction, forming the 'hinge' of the scissors (Figure 3). The protomer structure of the EC1-2 region is highly similar to the previously reported structure of a two-domain Pcdh-15 fragment, with an RMSD of 1.07 Å (Sotomayor et al., 2012). The only notable difference is a slight change in the position of the N-terminal helix, which appears to be displaced due to binding of Cdh23 in the earlier structure.

The structure of the Pcdh15 *cis* homodimer reveals a number of features that are atypical with respect to other published structures of cadherin superfamily proteins. The EC3 domain of Pcdh15 contains an embellishment to the typical cadherin fold where the A/A* strand connection

is interrupted by an inserted disulfide-stabilized A/A*-loop (Figure 4). The A/A*-loop from one protomer wraps around the back of its partner, as if the two protomers are embracing each other.

Importantly, while the EC1/EC2 linker region contains the canonical arrangement with three bound calcium ions, the EC2/EC3 junction did not contain electron density for Ca1. To confirm the absence of Ca1, we collected a low-energy x-ray anomalous scattering dataset to visualize Ca^{2+} in Bijvoet difference maps. Inspection of the Bijvoet difference maps revealed the three expected peaks in the Pcdh15 EC1/EC2 junction region, corresponding to the canonical binding of three Ca^{2+} ions (Figure S4A). However, the Bijvoet difference maps showed only two peaks in the Pcdh15 EC2/EC3 junction, corresponding to only two calcium ions bound at this non-canonical site (Figure S4B).

The Pcdh15 homodimer interface buries 740 $Å^2$ of interfacial surface area per protomer. While burying a relatively small surface area, the interface has high calculated shape complementarity (S_c) of 0.702. For comparison, the *trans* interface between Pcdh15 EC 1-2 and Cdh23 EC 1-2 buries 907 $Å^2$ and has an S_c of 0.511. The interface can be divided into two functional regions, one which is dominated by interactions between partner EC2/EC3 linker regions and the other which is located between the extended disulfide-stabilized A/A*-loop of one protomer and the surface formed by the C, F, and G β-strands of EC3 in the partner molecule (Figure 4). The EC2/EC3 junction sub-region contains hydrophobic interactions in which residues Leu138, Pro140, and Leu354 interact with copies of themselves across the 2-fold symmetry axis. Additionally, His352 from one protomer associates with Arg198 in the other through a cation-π interaction. Val250 in the A/A*-loop of one protomer forms interactions with a hydrophobic patch on the partner protomer lined by Leu306, Val307, and Val343. Additional interactions include a salt bridge formed between Asp255 and Lys345, and a cation-π interaction

formed between Arg257 and Phe357 (Figure 4B). Interestingly, though not identified by the authors, this interface exists in an already published crystal structure of Pcdh15 EC3-5 (PDB 5T4M), with an RMSD of 1.73 Å, providing additional support for its biological relevance (Figure S5) (Powers et al., 2017).

We also observe a number of sugar decorations, particularly on the adhesive domains. Pcdh15 EC1 contains two N-linked glycans, one on Asn31 and the other on Asn76; EC2 has a single N-glycan at Asn180. Cadherins and protocadherins are among a small number of protein families known to be modified by the addition of single O-mannose moieties to threonine residues (Vester-Christensen et al., 2013). Five threonine residues in Pcdh15 EC2 were modified by single O-mannose moieties: Thr144, Thr225, Thr227, Thr229, and Thr231 (Figure S6). The last four of these O-mannosylated residues are all on the G-strand of EC2 and are arranged in a single row of mannose moieties on the molecular surface. It is interesting that numerous cadherins and protocadherins have O-man sites clustered in EC2. Nevertheless, the functional role of O-mannosylation is not yet well understood. While the structure shows that O-man is likely to play no role in either *cis* or *trans* recognition, our data do not shed further light on other possible functions.

Point-mutations that interfere with *cis* dimerization

To biophysically validate the homodimer interface observed in the Pcdh15 EC1-3 structure, we produced several point mutations designed to disrupt the interface, and subjected these mutant proteins to analysis by both AUC and surface plasmon resonance (SPR) to assess their dimer-formation properties.

We designed targeted mutations in both parts of the Pcdh15 EC1-3 *cis* interface: in the interface between EC2/EC3-linker regions, and the EC3/EC3 interface between the extended A/A* loop and the body of the EC3 protomer (Figure 4). To target the EC2/EC3-linker interface, we mutated Leu138 and Arg198 to various amino acids. Leu138, near the *cis*-dimer two-fold axis, interacts with a copy of itself across the two-fold symmetry axis through hydrophobic interactions. Leu138Ala, Leu138Asp, and Leu138Phe mutations were designed to remove hydrophobic surface area, to introduce like-charge repulsion, or to cause steric clashing, respectively. Arg198Ala was designed to destabilize the interaction observed between Arg198 and His352.

To disrupt the EC3/EC3 protomer interface, Val250, Asp255 and Lys345 were mutated to disrupt interactions between the A/A* loop and the body of the EC3 domain. Val250Asp on the A/A* loop was chosen to disrupt the interface by burying a charged residue in a natively hydrophobic region. Asp255Lys, Lys345Ala, and Lys345Asp were designed to disrupt the salt bridge observed between Lys 345 and Asp 255.

AUC analysis revealed each of these *cis*-interface-targeted point mutants to show a significant decrease in dimerization affinity, with most showing no detectable homodimerization. Leu138Ala, Leu138Asp, Arg198Ala, Val250Asp, Asp255Lys, Lys345Ala, and Lys345Asp were all monomeric in solution. Leu138Phe failed to fully disrupt dimerization, but showed attenuated binding, with a K_D of 15.3 μM, as compared to 1.2 μM for wild-type (Table S2).

We also performed SPR experiments in which wild-type Pcdh15 EC1-3 was immobilized on the chip surface, and interactions between wild-type and mutant protein analytes were assessed (Figure 5). As expected, the greatest binding response was elicited when wild-type Pcdh15 EC1-3 was flowed over the chip surface; no binding was detected when Pcdh15 EC1-2,

lacking EC3, was used as the analyte, and all point mutants showed attenuated binding responses, compared to wild type (Figure 5). Of the mutant proteins, Leu138Phe generated SPR binding curves with a maximum response closest to the wild-type curves, which is consistent with its inability to disrupt dimerization in AUC. Val250Asp showed the strongest inhibition of *cis* dimerization in the SPR experiments (Figure 5B).

We next attempted to determine the effects of these mutations on dimerization in the context of the larger Pcdh15 ectodomain. Since the PICA domain mediates *cis* dimerization, all PICA domain-containing constructs were dimeric. We therefore introduced the EC2/EC3 *cis*-interface region mutations in the context of an eleven-domain construct, which includes all EC domains of Pcdh15, but lacks the PICA domain. Wild-type Pcdh15 EC1-11 formed dimers with 1.8 μM affinity in solution as assessed by AUC. Pcdh15 EC1-11 Arg198Ala appeared dimeric in AUC experiments, but partial precipitation during the experiment prevented us from calculating a K_D with confidence; Pcdh15 EC1-11 Val250Asp, however, was monomeric, both in AUC and negative-stain TEM (Figure S8). Taken together, these results indicate that while a majority of the binding energy derives from the EC2-3 interface observed in the crystal structure, the rest of the ectodomain does contribute to dimerization, but with binding energy too low to be detected by AUC.

Validation of cis-dimerization interface by charge-reversal experiments

We sought to demonstrate definitively that the effects observed from targeted mutation of Asp255 and Lys345 resulted from disruption of a salt bridge between them; to accomplish this, we employed a strategy using charge-reversal experiments. Asp255Lys and Lys345Asp mutations were designed to introduce like-charge repulsion in homogenous populations of either

mutant, yet, as they should compensate for one another, *cis* heterodimers are expected to form when the two mutant proteins are mixed together. Each of these mutant proteins is monomeric in solution. To determine whether these two mutations compensate each other as predicted, we performed SPR experiments in which each mutant protein was immobilized on the chip surface. These surfaces showed no measurable binding for wild-type Pcdh15 EC1-3 or for other non-compensatory mutations (Figure 5C). The Lys345Asp surface, however, showed robust binding to Asp255Lys; similarly, the Asp255Lys surface showed robust binding to Lys345Asp, as well as some moderate binding to Lys345Ala, possibly as a result of the mutation permitting a new salt bridge to form with Glu347 (Figure 5C). These charge-reversal experiments show that the *cis* dimerization mode we observe crystallographically indeed represents the biophysically observed dimer.

We also generated a select few Pcdh15 EC1-3 double mutants and one triple mutant and analyzed their oligomeric state using size exclusion chromatography (Figure S7). Leu138Ala/Asp255Lys eluted predominately as a monomer, as expected. Leu138Ala/Lys345Asp eluted as a mixed population with a slightly higher monomer peak. Asp255Lys/Lys345Asp eluted predominately as a dimer, which is in agreement with the SPR data for the two complementary salt bridge mutations. Lastly, the Leu138Ala/Asp255Lys/ Lys345Asp eluted primarily as a monomer, with a small shoulder corresponding to the dimer.

Single Particle Reconstruction From Negative Stain Electron Microscopy

We next used single-particle negative-stain EM and 3D reconstruction to visualize the ectodomain of Pcdh15. We separately imaged both the full-length ectodomain, which as described below was complicated by aggregation mediated by the PICA domain, as well as a

Pcdh15 EC1-11 protein lacking the PICA domain. Particles were picked via template picking with FindEM (Roseman, 2004) and 2D class averages were generated using RELION (Kimanius et al., 2016). The 2D class averages were of sufficient resolution so that most individual EC domains are resolved; overall, the class averages clearly show a Pcdh15 dimer arranged as a parallel double helix (Figure 6A). Toward one end of the dimer is a region of increased electron density for two successive domains (blue arrow), which corresponds to the EC3 *cis*-dimer interface observed in the crystal structure. Two lobes, corresponding to the EC1-2 Cdh23-interacting regions, can be seen adjacent to these EC2-3 dimerization regions in many of the 2D classes. Notably, for the Pcdh15 EC1-11 protein, slight feathering is observed at the opposite EC11-proximal end, indicating flexibility or conformational heterogeneity, which is not surprising in the absence of *cis*-dimeric PICA domain.

We used the program cryoSPARC (Punjani et al., 2017)to reconstruct a 3D map to 20 Å nominal resolution. The positions of individual EC domains are clear in this map, enabling us to position the structure of Pcdh15 EC1-3 dimer, and also to place 7 additional EC domains for each monomer using a model of the EC3 domain from N-cadherin, such that the positions of 10 EC domains in total were modeled for each Pcdh15 monomer (Figure 6B). The final EC domain could not be modeled, likely due to the apparent disorder at the C-terminal end evident as feathering in the 2D class averages. The model generated is that of a right-handed, parallel double helix. The overall dimensions of the *cis*-dimeric structure of the Pcdh15 ectodomain, with 10 visualized EC domains per protomer, is ~485 Å in total length, with a helix diameter of ~85 Å. The 10-domain structure completes ~0.5 helical turns; thus, the helical rise per turn is ~690 Å. This is in agreement with the helical rise measured in Kachar et al (2000). Importantly, this structure is for Pcdh15 under zero tension; thus the helix winding is expected to be near its

maximum. At 20Å nominal resolution, only the overall domain positions are defined. We therefore view this model as defining the overall architecture of Pcdh15, however given the low resolution, we hesitate to extract details from the model beyond its overall dimensions.

We also produced a construct of the full ectodomain (EC1-PICA) for imaging by single-particle negative stain EM. As before, Particles were picked manually and 2D class averages were generated using RELION. However, far fewer isolated particles could be obtained due to the formation of higher order oligomers. These oligomers, which were directly visualized in EM images, show associations between Pcdh15 dimers forming through the PICA domain region. Nonetheless, we were able to generate 2D class averages of Pcdh15 EC1-PICA (Figure 6C). Similar to the Pcdh15 EC1-11 protein, the overall orientation of the Pcdh15 ectodomain was clear in the class averages due to the distinctive structures at either end of the molecule. The Cdh23-interacting N-terminal end appears as a forked bi-lobed structure. Unlike the EC1-11 structure, where the C-terminal end is monolithic and becomes increasingly disordered, in the PICA domain containing structure, the C-terminal end instead culminates in a bright region corresponding to the dimeric PICA domain. Indeed, the most notable difference between the two sets of class averages is the dramatically reduced amount of feathering in the PICA domain-containing full-length ectodomain. This is consistent with our biophysical results showing that the PICA domain provides an additional mediator of membrane-proximal *cis* dimerization.

Mutations that affect Pcdh15 homodimerization perturb its function in hair cells

We have previously shown that injectoporation is a useful method to express the genetically encoded Ca^{2+} sensor G-CaMP3 in hair cells and to then analyze mechanotransduction by changes in the fluorescence intensity of G-CaMP3 following stimulation of hair bundles with

a fluid jet (Figure 7B) (Xiong et al., 2012; Xiong et al., 2014; Zhao et al., 2014). To determine the extent to which Pcdh15 homodimerization is critical for its function in hair cells, we used injectoporation to express recombinant Pcdh15 molecules carrying point mutations together with G-CaMP3 in hair cells from Pcdh15-deficient homozygous *Ames-waltzer*^{av3J} mice (Alagramam et al., 2001) and measure effects of the mutations on transduction. We engineered mutations that alter one, two, or three amino acids in the EC2/EC3 dimerization domain (Arg198Ala, Val250Asp, Leu138Ala, Asp255Lys, Lys345Asp; Leu138Ala/Asp255Lys, Leu138Ala/Lys345Asp; Leu138Ala/Asp255Lys/Lys345Asp) in full length Pcdh15 (Figure 7A). To test that the mutations did not interfere with cell surface expression, we next transfected the constructs containing an HA-tag at the C-terminus into HEK293 cells together with LHFPL5, which is necessary for efficient expression of wild-type Pcdh15 at the cell surface (Xiong et al. 2012). We then biotinylated proteins at the cell-surface, prepared extracts and immunoprecipitated Pcdh15 with HA antibodies. Western blotting with antibodies to HA demonstrated that all constructs were efficiently expressed in HEK293 cells with the exception of Val250Asp, which was consistently expressed at lower levels (Figure 7C). Analysis of cell surface expressed protein with streptavidin coupled detection reagents revealed that all proteins were expressed at the cell surface with similar efficiency, with the exception of Val250Asp, which was present at lower levels (Figure 7D). However, relative to total levels of Pcdh15-Val250Asp, the mutant construct was expressed more efficiently at the cell surface compared to wild-type Pcdh15 (Figure 7D).

Next, we expressed by injectoporation Pcdh15 constructs in hair cells. For this experiment we used Pcdh15 constructs lacking the epitope tag. Efficient expression of mutant constructs was observed in hair bundles using immunolocalization experiments (Figure 7E,F).

For a quantitative assessment of expression levels, we used Imaris 9.1 software to generate 3D reconstructions of hair bundles that were stained with phalloidin to reveal their F-actin cytoskeleton. Pcdh15 expression was detected with Pcdh15 antibodies (Figure 7E, bottom three panels). We determined the volume ratio of Pcdh15 staining and phalloidin staining (Figure 7F). There was no significant difference in expression levels for the different Pcdh15 mutants, even for Val250Asp, which was less efficiently expressed in heterologous cells compared to other Pcdh15 constructs (Figure 7F). Notably, the stereocilia that form the hair bundle of a hair cell are devoid of vesicles and transmembrane proteins in stereocilia are inserted into the plasma membrane near the base of stereocilia from where they are transported into stereocilia. Thus, the protein levels that we observed in the hair bundle likely reflects Pcdh15 levels at the cell surface and the data suggest that all constructs are expressed efficiently and at comparable levels in hair bundles of hair cells.

For functional studies, Ca^{2+} imaging was applied while hair bundles were mechanically stimulated with a fluid jet by applying three consecutive pulses of increasing duration (0.1, 0.3 and 0.5 sec). Hair cells from *Ames-waltzer*^{av3J} mice did not show any significant increase in fluorescence intensity following mechanical stimulation of their hair bundles (Figure 7G). In contrast, re-expression of wild-type Pcdh15, lead to a robust increase in fluorescence in response to mechanical stimulation of the bundle (Figure 7G). Next, we analyzed Pcdh15 molecules carrying different mutations in the EC2/EC3 *cis*-homodimerization interface. Although our biophysical experiments demonstrated that *cis*-dimerization is dependent not only on the EC2/EC3 interface but also on the PICA domain, we reasoned that weakening this structurally defined membrane-distal interface, which significantly contributes to *cis* dimerization, would lead to detectable functional impairment in the biologically relevant environment of hair cells.

For functional studies, we engineered both the Arg198Ala and Val250Asp mutations into full-length Pcdh15. Significantly, Pcdh15-Arg198Ala rescued mechanotransduction defects in hair cells from *Ames-waltzer*^{av3J} mice similar to wild-type Pcdh15, while Pcdh15-Val250Asp only restored transduction partially (Figure 7G) even though it was targeted to stereocilia (Figure 7F). Biophysical experiments show that, in an EC1-11 construct lacking the PICA domain, Val250Asp but not Arg198Ala perturbed *cis* dimerization between the 11 EC repeat fragment. These results are consistent with the requirement of *cis* dimerization for functional transduction.

For further verification of the dimerization interface, we also tested single mutations Leu138Ala, Asp255Lys and Lys345Asp; double mutations Leu138Ala/Asp255Lys and Leu138Ala/Lys345Asp; and the triple mutation Leu138Ala/Asp255Lys/Lys345Asp. Single-mutant constructs restored mechanical sensitivity to hair bundles from Pcdh15-deficient *Ames-waltzer*^{av3J} mice to a similar degree as wild-type Pcdh15 (Figure 7G), suggesting that single mutants were not sufficiently strong to disrupt dimerization in the presence of the remainder of the extracellular Pcdh15 domain including the PICA domain. However, double mutants were efficiently targeted to stereocilia (Figure 7C,D), but had significantly impaired Pcdh15 function (Figure 7G). Strikingly, triple-mutation constructs containing the charge reversal mutations Asp255Lys and Lys345Asp that should enable a salt bridge to form in the reverse orientation restored Pcdh15 function (Figure 7G). Taken together, these data suggest that mutations in the EC2/EC3 dimerization surface that weaken *cis* homodimerization of Pcdh15 affect its function in hair cells. Unfortunately, as we have so far not succeeded in obtaining crystals of the *cis*-homodimer interface within the PICA domain, structure-guided mutational analysis to test the function of amino acids critical for homophilic *cis*-interactions mediated by PICA domains remains out of reach.

DISCUSSION

The adhesion complex formed by Pcdh15 and Cdh23 in tip links of hair cells shows features different from other cadherin adhesion complexes, reflecting likely functional adaptations of tip-link cadherins for their role in mechanotransduction. *Cis* dimerization is predicted to affect the mechanical properties of tip links, providing stability through lateral *cis* interactions and by increasing the effective adhesive strength through formation of a dimeric *trans* interface. These features are expected to be critical for mechanotransduction by affecting the transfer of mechanical force to transduction channels, and by opposing rupture of the Pcdh15/Cdh23 *trans* bond during mechanical stimulation. Here we have used single-particle electron microscopy and solution biophysical measurements to gain insights into the overall architecture of the *cis*-dimeric Pcdh15 ectodomain, and x-ray crystallography to define at atomic resolution structural features of Pcdh15 that are critical for *cis* homodimerization. Our functional studies in hair cells provide evidence that disruption of the *cis*-homodimeric architecture of Pcdh15 affects its function in hair cells.

Our findings reveal a lateral interaction mode that drives *cis* dimerization, which has not been previously recognized for a member of the cadherin superfamily. This lateral interaction leads to the formation of a *cis*-dimeric double helical filament. The Pcdh15 EC domain region (EC1-11) forms a parallel double-helical dimer ~485Å in length from the first cadherin domain EC1 to EC10, the final well-ordered domain in the reconstruction, making ~0.5 helical turns in total. The membrane-proximal PICA domain and the preceding EC11 domain will add to this length in the complete ectodomain. Two *cis*-dimeric interfaces are present in the Pcdh15 ectodomain: one that forms through the membrane-proximal PICA domain, and the other encompassing regions of domains EC2 and EC3. Thus, the overall architecture of the Pcdh15

ectodomain is a parallel double-helical dimer bridged in *cis* by two distinct interfaces distal from one another. The *cis*-dimeric architecture of Pcdh15 defined here, combined with a prior structure of the *trans* interaction of Pcdh15 with Cdh23, allows us to model the interaction region of the native 2:2 complex (Figure 8), and shows that the Pcdh15 *cis* dimer can accommodate the known *trans* binding mode with Cdh23 positioned internally (toward the *cis*-dimer 2-fold axis) relative to Pcdh15.

Biophysical studies have revealed the existence of a gating spring which is critical for gating transduction channels in hair cells. Tip links have been proposed to function both in the conveyance of force and as a gating spring for the transduction channel (Corey and Hudspeth, 1983; Howard and Hudspeth, 1987; Pickles et al., 1984). It is still unclear whether the tip link contributes to the gating spring, or if the gating spring is provided by one or more molecules connected in series to the tip link. Earlier structural studies of Cdh23 and Pcdh15 have focused on the question of tertiary structural elasticity – whether force applied to Pcdh15 will result in protein extension without unfolding (Araya-Secchi et al., 2016; Powers et al., 2017; Sotomayor et al., 2010, 2012). In these studies, Sotomayor and coworkers have reported crystal structures for monomeric EC domain pairs or triples produced in *E. coli*, and computationally assessed the spring properties of these *cis*-monomeric ectodomain fragments using steered molecular dynamics. *In silico* simulation of monomeric protein fragments encompassing the EC1 and EC2 domains of Cdh23 was reported to suggest that tip links might be too stiff to function as the gating spring, a hypothesis that was initially based on the observed double-stranded nature of the tip link (Kachar et al., 2000; Sotomayor et al., 2010). However, subsequent studies suggested that only some regions of the tip link might be too stiff to act as the gating spring, whereas other regions could potentially elongate significantly in response to force (Araya-Secchi et al., 2016;

Powers et al., 2017; Sotomayor et al., 2012). These conclusions were based on crystal structures of Pcdh15 ectodomain fragments EC1-2, EC3-5, EC8-10, and EC9-10 (Araya-Secchi et al., 2016; Powers et al., 2017; Sotomayor et al., 2010, 2012). Steered molecular dynamics simulations were used to generate force extension curves, which suggested that each of these fragments were too stiff to extend significantly under forces of the magnitude experienced by the tip link. One structural element, however, a bent connection between the successive domains EC9 and EC10, could be extended by straightening the bend at physiological levels of force (Araya-Secchi et al., 2016). Straightening this EC9-10 bend was postulated to mediate lengthening of Pcdh15 by up to 4 nm.

Our structural studies now provide insight into structural features of the entire Pcdh15 ectodomain, which indicate additional potential for structural flexibility. While some modes of Pcdh15 elasticity might depend on effects that can be understood by investigating sub-regions in isolation, others may depend on its overall quaternary structure. One potential mode of structural elasticity that becomes apparent in light of the overall structure of Pcdh15 we describe here is elongation in response to force through helix unwinding. Since the two molecules of the *cis* dimer are bridged by two interfaces distal from one another and which comprise only a fraction of the available molecular surface area, molecular elasticity is perhaps provided by unwinding and rewinding of the Pcdh15 double helix. We estimated the maximum elongation possible through helix unwinding, both by measuring the distance traversed through the helical electron density of one molecule, and by with the equation for helix path length, $L = (\text{HelixRise}^2 + \text{Circumference}^2)^{1/2}$, and obtained similar values. In a completely unwound state, this helical path could in principle be straightened to elongate the molecule from ~485 Å – the length we measure from the zero-tension single-particle reconstructions – to ~520 Å in length, yielding an extension

of ~35 Å. Pcdh15 accounts for about one third the length of the tip link (11 EC domains plus the PICA domain), with about two-thirds in cadherin 23 (27 EC domains) – also a giant cadherin that appears in freeze etched EM images and in low-resolution negative staining EM images to form a tightly wound helix (Kachar et al., 2000; Kazmierczak et al., 2007). Thus, a helical tip link consisting of 38 EC domains and a PICA domain might have significant structural flexibility through helix unwinding and rewinding that goes well beyond the 6 nm upper limit defined so far by structural studies of Pcdh15. Notably, tip links in hair cells at rest already experience substantial force. Measurements in bullfrog suggest a resting force of approximately 8 pN (Jaramillo and Hudspeth, 1993). With a gating spring stiffness of 500 uN/m, the spring would already be extended at rest by ~16 nm (Jaramillo and Hudspeth, 1993) and helix unwinding might substantially contribute to this extension.

In experimental settings, gating springs can extend under extreme conditions by as much as ~150 nm (Shepherd and Corey, 1994), a range that far exceeds the dimensions possible with flexibility in the EC9-10 region and helix unwinding. However, hair bundles in vivo are extraordinarily sensitive to deflection, responding maximally to ~1° angular deflection (Corey and Hudspeth, 1983). At the threshold of hearing, bundles are deflected by less than 1 nm (Rhode and Geisler, 1967). Thus, the gating spring likely extends far less than 150 nm under physiologically relevant conditions. To accomplish extensions in the order of 150 nm by elongation of Pcdh15 and Cdh23 alone would likely require protein unfolding. One mode of extension that has been proposed involves β-strands "popping out" of individual EC domains to add length to the tip link (Powers et al., 2017; Sotomayor et al., 2010). Arguing against this idea is the slow kinetics expected for refolding, which could significantly limit response times expected to be faster than 50 μs. To accommodate extension on the order of 150 nm therefore

likely involves other elements, potentially including the cell membrane. Notably, the persistence of the tip link under extreme mechanical deflection suggests that the specific *trans*-adhesive interface formed between the *cis* homodimer of Pcdh15 and the *cis* homodimer of Cdh23 is exceptionally strong.

In summary, our findings provide first insights into the *cis*-homodimeric structure of the Pcdh15 ectodomain and reveal unique mechanisms of lateral dimerization not observed for any other cadherin. It will be interesting to determine whether other members of the cadherin superfamily can adopt a helix conformation similar to Pcdh15. For example, Pcdh24 has been shown to be a component of intermicrovillar adhesions in intestinal brush border cells (Crawley et al., 2014). Intriguingly, the ectodomain of Pcdh24 shares features with tip-link cadherins (Elledge et al., 2010; Sotomayor et al., 2010). Like in Pcdh15 and Cdh23, the Pcdh24 ectodomain is substantially larger than in classical cadherins. It also lacks N-terminal tryptophan residues in EC1, which are critical for *trans* interactions between classical cadherins (Boggon et al., 2002; Shan et al., 1999; Shapiro et al., 1995), suggesting possible similarities in structural organization and trans binding. It will thus be important to determine ectodomain structures for other atypical members of the cadherin superfamily. We anticipate that the structural organization that we describe here will apply to other cadherins thus defining a subfamily within the larger superfamily with potentially shared functions.

Acknowledgements

We thank Surajit Banerjee and Igor Kourinov for help with synchrotron data collection conducted at the APS NE-CAT 24-ID-C beamline, which is supported by National Institutes of Health (NIH) P41 GM103403. We acknowledge the support of a National Science Foundation grant (MCB-1412472) to B.H., and a joint NIH grant (R01DC016960) to U.M. and L.S. G.D.

was supported by an NIH training grant. The computing in this project was supported by two NIH instrumentation grants (S10OD012351 and S10OD021764) received by the Department of Systems Biology at Columbia University. Electron microscopy was performed at the Simons Electron Microscopy Center and National Resource for Automated Molecular Microscopy located at the New York Structural Biology Center, supported by grants from the Simons Foundation (349247), NYSTAR, and the NIH National Institute of General Medical Sciences (GM103310) with additional support from Agouron Institute (Grant Number: F00316) and NIH S10 OD019994-01.

Author contributions

G.D., X.Q., C.S.P., B.C., B.H., U.M. and L.S. designed experiments and analyzed data; M.A.R. performed electron microscopy experiments; X.Q. carried out functional studies in hair cells; X.L. analyzed Pcdh15 expression in heterologous cells; B.Z. and G. P. cloned Pcdh15 expression constructs. P.S.K. performed SPR experiments; G.A. performed analytical ultracentrifugation experiments; R.R. performed sequence alignments; G.D. produced proteins and performed crystallography experiments. G.D., U.M. and L.S. wrote the paper.

Declaration of Interests

The authors declare no competing interests.

REFERENCES

Ahmed, Z.M., Goodyear, R., Riazuddin, S., Lagziel, A., Legan, P.K., Behra, M., Burgess, S.M., Lilley, K.S., Wilcox, E.R., Riazuddin, S.*, et al.* (2006). The tip-link antigen, a protein associated with the transduction complex of sensory hair cells, is protocadherin-15. The Journal of neuroscience : the official journal of the Society for Neuroscience *26*, 7022-7034.

Ahmed, Z.M., Riazuddin, S., Bernstein, S.L., Ahmed, Z., Khan, S., Griffith, A.J., Morell, R.J., Friedman, T.B., Riazuddin, S., and Wilcox, E.R. (2001). Mutations of the protocadherin gene PCDH15 cause Usher syndrome type 1F. American journal of human genetics *69*, 25-34.

Alagramam, K.N., Yuan, H., Kuehn, M.H., Murcia, C.L., Wayne, S., Srisailpathy, C.R., Lowry, R.B., Knaus, R., Van Laer, L., Bernier, F.P.*, et al.* (2001). Mutations in the novel protocadherin PCDH15 cause Usher syndrome type 1F. Hum Mol Genet *10*, 1709-1718.

Araya-Secchi, R., Neel, B.L., and Sotomayor, M. (2016). An elastic element in the protocadherin-15 tip link of the inner ear. Nature communications *7*, 13458.

Assad, J.A., Shepherd, G.M., and Corey, D.P. (1991). Tip-link integrity and mechanical transduction in vertebrate hair cells. Neuron *7*, 985-994.

Boggon, T.J., Murray, J., Chappuis-Flament, S., Wong, E., Gumbiner, B.M., and Shapiro, L. (2002). C-cadherin ectodomain structure and implications for cell adhesion mechanisms. Science *296*, 1308-1313.

Bolz, H., von Brederlow, B., Ramirez, A., Bryda, E.C., Kutsche, K., Nothwang, H.G., Seeliger, M., del, C.S.C.M., Vila, M.C., Molina, O.P.*, et al.* (2001). Mutation of CDH23, encoding a new member of the cadherin gene family, causes Usher syndrome type 1D. Nature genetics *27*, 108-112.

Corey, D.P., and Hudspeth, A.J. (1983). Kinetics of the receptor current in bullfrog saccular hair cells. J Neurosci *3*, 962-976.

Crawley, S.W., Shifrin, D.A., Jr., Grega-Larson, N.E., McConnell, R.E., Benesh, A.E., Mao, S., Zheng, Y., Zheng, Q.Y., Nam, K.T., Millis, B.A.*, et al.* (2014). Intestinal brush border assembly driven by protocadherin-based intermicrovillar adhesion. Cell *157*, 433-446.

Edelstein, A., Amodaj, N., Hoover, K., Vale, R., and Stuurman, N. (2010). Computer control of microscopes using microManager. Curr Protoc Mol Biol *Chapter 14*, Unit14 20.

Elledge, H.M., Kazmierczak, P., Clark, P., Joseph, J.S., Kolatkar, A., Kuhn, P., and Muller, U. (2010). Structure of the N terminus of cadherin 23 reveals a new adhesion mechanism for a subset of cadherin superfamily members. Proceedings of the National Academy of Sciences of the United States of America *107*, 10708-10712.

Harrison, O.J., Jin, X., Hong, S., Bahna, F., Ahlsen, G., Brasch, J., Wu, Y., Vendome, J., Felsovalyi, K., Hampton, C.M.*, et al.* (2011). The extracellular architecture of adherens junctions revealed by crystal structures of type I cadherins. Structure *19*, 244-256.

Howard, J., and Hudspeth, A.J. (1987). Mechanical relaxation of the hair bundle mediates adaptation in mechanoelectrical transduction by the bullfrog's saccular hair cell. Proc Natl Acad Sci U S A *84*, 3064-3068.

Hudspeth, A.J. (2014). Integrating the active process of hair cells with cochlear function. Nature reviews Neuroscience *15*, 600-614.

Hudspeth, A.J., and Jacobs, R. (1979). Stereocilia mediate transduction in vertebrate hair cells (auditory system/cilium/vestibular system). Proceedings of the National Academy of Sciences of the United States of America *76*, 1506-1509.

Indra, I., Choi, J., Chen, C.S., Troyanovsky, R.B., Shapiro, L., Honig, B., and Troyanovsky, S.M. (2018). Spatial and temporal organization of cadherin in punctate adherens junctions. Proceedings of the National Academy of Sciences of the United States of America *115*, E4406-E4415.

Jaramillo, F., and Hudspeth, A.J. (1993). Displacement-clamp measurement of the forces exerted by gating springs in the hair bundle. Proc Natl Acad Sci U S A *90*, 1330-1334.

Kachar, B., Parakkal, M., Kurc, M., Zhao, Y., and Gillespie, P.G. (2000). High-resolution structure of hair-cell tip links. Proceedings of the National Academy of Sciences of the United States of America *97*, 13336-13341.

Kazmierczak, P., Sakaguchi, H., Tokita, J., Wilson-Kubalek, E.M., Milligan, R.A., Muller, U., and Kachar, B. (2007). Cadherin 23 and protocadherin 15 interact to form tip-link filaments in sensory hair cells. Nature *449*, 87-91.

Kimanius, D., Forsberg, B.O., Scheres, S.H., and Lindahl, E. (2016). Accelerated cryo-EM structure determination with parallelisation using GPUs in RELION-2. Elife *5*.

Pan, B., and Holt, J.R. (2015). The molecules that mediate sensory transduction in the mammalian inner ear. Current opinion in neurobiology *34*, 165-171.

Pepermans, E., and Petit, C. (2015). The tip-link molecular complex of the auditory mechano-electrical transduction machinery. Hearing research *330*, 10-17.

Pickles, J.O., Comis, S.D., and Osborne, M.P. (1984). Cross-links between stereocilia in the guinea pig organ of Corti, and their possible relation to sensory transduction. Hear Res *15*, 103-112.

Powers, R.E., Gaudet, R., and Sotomayor, M. (2017). A Partial Calcium-Free Linker Confers Flexibility to Inner-Ear Protocadherin-15. Structure *25*, 482-495.

Punjani, A., Rubinstein, J.L., Fleet, D.J., and Brubaker, M.A. (2017). cryoSPARC: algorithms for rapid unsupervised cryo-EM structure determination. Nat Methods *14*, 290-296.

Rhode, W.S., and Geisler, C.D. (1967). Model of the displacement between opposing points on the tectorial membrane and reticular lamina. J Acoust Soc Am *42*, 185-190.

Ricci, A.J., Kachar, B., Gale, J., and Van Netten, S.M. (2006). Mechano-electrical transduction: new insights into old ideas. The Journal of membrane biology *209*, 71-88.

Roseman, A.M. (2004). FindEM--a fast, efficient program for automatic selection of particles from electron micrographs. J Struct Biol *145*, 91-99.

Shan, W.S., Koch, A., Murray, J., Colman, D.R., and Shapiro, L. (1999). The adhesive binding site of cadherins revisited. Biophys Chem *82*, 157-163.

Shapiro, L., Fannon, A.M., Kwong, P.D., Thompson, A., Lehmann, M.S., Grubel, G., Legrand, J.F., Als-Nielsen, J., Colman, D.R., and Hendrickson, W.A. (1995). Structural basis of cell-cell adhesion by cadherins. Nature *374*, 327-337.

Shepherd, G.M., and Corey, D.P. (1994). The extent of adaptation in bullfrog saccular hair cells. J Neurosci *14*, 6217-6229.

Siemens, J., Lillo, C., Dumont, R.A., Reynolds, A., Williams, D.S., Gillespie, P.G., and Muller, U. (2004). Cadherin 23 is a component of the tip link in hair-cell stereocilia. Nature *428*, 950-955.

Sotomayor, M., Weihofen, W.A., Gaudet, R., and Corey, D.P. (2010). Structural determinants of cadherin-23 function in hearing and deafness. Neuron *66*, 85-100.

Sotomayor, M., Weihofen, W.A., Gaudet, R., and Corey, D.P. (2012). Structure of a force-conveying cadherin bond essential for inner-ear mechanotransduction. Nature *492*, 128-132.

Vester-Christensen, M.B., Halim, A., Joshi, H.J., Steentoft, C., Bennett, E.P., Levery, S.B., Vakhrushev, S.Y., and Clausen, H. (2013). Mining the O-mannose glycoproteome reveals cadherins as major O-mannosylated glycoproteins. Proceedings of the National Academy of Sciences of the United States of America *110*, 21018-21023.

Webb, S.W., Grillet, N., Andrade, L.R., Xiong, W., Swarthout, L., Della Santina, C.C., Kachar, B., and Muller, U. (2011). Regulation of PCDH15 function in mechanosensory hair cells by alternative splicing of the cytoplasmic domain. Development *138*, 1607-1617.

Xiong, W., Grillet, N., Elledge, H.M., Wagner, T.F., Zhao, B., Johnson, K.R., Kazmierczak, P., and Muller, U. (2012). TMHS is an integral component of the mechanotransduction machinery of cochlear hair cells. Cell *151*, 1283-1295.

Xiong, W., Wagner, T., Yan, L., Grillet, N., and Muller, U. (2014). Using injectoporation to deliver genes to mechanosensory hair cells. Nat Protoc *9*, 2438-2449.

Zhao, B., and Muller, U. (2015). The elusive mechanotransduction machinery of hair cells. Current opinion in neurobiology *34*, 172-179.

Zhao, B., Wu, Z., Grillet, N., Yan, L., Xiong, W., Harkins-Perry, S., and Muller, U. (2014). TMIE Is an Essential Component of the Mechanotransduction Machinery of Cochlear Hair Cells. Neuron *84*, 954-967.

FIGURE TITLES AND LEGENDS

Figure 1. Diagram of a hair bundle of a mechanosensory hair cell.

(A) Overview of the hair bundle indicating the tip link.

(B) The double-helical tip link is a homodimer of Pcdh15 interacting in *trans* with a homodimer of Cdh23. The mechanically gated ion channel (channel complex) is located at the lower end of tip links. Several proteins such as harmonin, SANS, MYO7A and MYO1C are located at the upper end of the tip link.

Figure 2. Schematic of protein fragments used to interrogate Pcdh15 for *cis* dimeric interactions.

Two, three, and four domain constructs were cloned, expressed, and analyzed via AUC-SE experiments to check for homodimerization, see also Figure S1 and Table S2. A Pcdh15 fragment containing the PICA domain was analyzed by MALS, see also Figures S2 and S3. Proteins that formed dimers are colored light blue, while monomers are colored tan. Constructs that did not express are colored in grey.

Figure 3. Structure of the Pcdh15 EC1-EC3 *cis* dimer.

Pcdh15 EC1-EC3 *cis* dimer forms through a surface that spans the EC2-EC3 linker region, the "top" of EC3, and the disulfide-stabilized loop formed by an inserted segment between the A and A' strands of EC3. This interface is also present, yet not described, in a previously published structure of Pcdh15 EC3-EC5 (PDB ID: 5T4M, see also Figure S5). Calcium ions are represented as green spheres (see also Figure S4), and glycans as red, white and blue spheres (see also Figure S6).

Figure 4. Structural details of the *cis* dimer interface

(A) Expanded views of the cis-dimer interface, with details of the EC2-3 junction interface (upper panel) and the EC3-EC3 interface (lower panel).

(B) Interfacial residues shown on a single Pcdh15 protomer.

Figure 5. Surface Plasmon Resonance binding curves for point-mutants in the Pcdh15 *cis* interface.

(A) SPR response curves for mutations targeting the EC2-3 interface through residue Leu138.

(B) SPR response curves for mutations targeting Arg198 in the EC2-3 interface and Val250 in the EC3-EC3 interface.

(C) SPR response curves for mutations targeting the Asp255/Lys345 salt bridge in the EC3-EC3 interface, showing disruption of binding (upper panel) and rescue through complementation (lower two panels). See also Figure S7.

Figure 6. 2D Class Average and a 3D Reconstruction of negative stain Electron Micrographs

(A) 2D Class averages of WT Pcdh15 EC1-11 from negative stain Electron Micrographs. The number of individual images used is presented at the base of the image. See also Figure S8.

(B) 3D class average generated from negative stain. Manually placed into the density for reference is the crystal structure of Pcdh15 EC1-3, as well as simulated 11Å electron density for an additional 14 cadherin domains.

(C) 2D Class averages of WT Pcdh15 EC1-PICA from negative stain Electron Micrographs

Figure 7. Functional characterization of Pcdh15 mutants in hair cells.

(A) Diagram of the Pcdh15 homodimer. Mutations used in functional studies are indicated.

(B) Diagram of the injectoporation procedure. Cochlear explants are injected with plasmid solution and the plasmid is transferred into hair cells by electroporation.

(C) HEK293 cells were transfected to express wild-type and mutant Pcdh15 constructs that contained a C-terminal HA-tag (Pcdh15-HA). Myc-LHFPL5 was co-expressed to achieve efficient Pcdh15 cell surface expression (Xiong et al. 2012). Where indicated, protein at the cell surface were biotinylated. Protein extracts were prepare and immunoprecipitated (IP) with antibodies to HA. Pcdh15-HA was detected by western blotting (IB) using streptavidin-conjugated detection reagent (Bio- Pcdh15) or antibodies to HA (Pcdh15-HA). The lower lanes show input protein prior to immunoprecipitation detected with antibodies to HA or Myc or Transferrin Receptor (TFR) (loading control).

(D) Levels of Pcdh15-HA at the cell surface were determined by densitometric scanning of gels from three independent experiments. Values are expressed as a ratio between total levels versus levels at the cell surface, where levels for wild-type Pcdh15-HA are set at 1. All data are mean ± SEM. Student's two-tailed unpaired t test was used to determine statistical significance (*, $p<0.05$, **, $p<0.01$, ***, $p<0.001$).

(E) Hair cells at P3 were injectoporated to express the indicated Pcdh15 constructs without and HA tag. Hair cells were stained two days later with phalloidin (red) and with antibodies to Pcdh15 (green). Both wild-type and mutant Pcdh15 were targeted to stereocilia. The lowest three panels show 3D rendering (Imaris 9.1) of a hair bundle expressing wild-type Pcdh15 (red) where the hair bundle was visualized with phalloidin (green). A front side and back view of a hair bundle is shown.

(F) Quantification of expression levels of Pcdh15 constructs in hair bundles by determining the volume ratio of Pcdh15 staining and phalloidin staining. The number of quantified

hair bundles is indicated. All values are mean ± SEM. Student's two-tailed unpaired t test was used to determine statistical significance (∗, $p < 0.05$, ∗∗, $p < 0.01$, ∗∗∗, $p < 0.001$).

(G) Hair cells from homozygous *Ames-waltzer*^{av3J} mice were injectoporated at P2 to express GCaMP3 and the indicated Pcdh15 constructs. After 2 days in culture, mechanotransduction was evaluated by deflecting hair bundles for increasing amounts of time while simultaneously measuring increases in GCaMP3 fluorescence. On the right, representative traces are shown for individual constructs. The number of analyzed cells is indicated. On the right, the amplitude of the 2nd Ca^{2+} response peak was quantified. All data are mean ± SEM. Student's two-tailed unpaired t test was used to determine statistical significance (*, $p<0.05$, **, $p<0.01$, ***, $p<0.001$).

Figure 8. Model of Pcdh15 EC1-3 in complex with Cdh23 EC1-2

A model of Cdh23 EC1-2, in lilac, in complex with the Pcdh15 EC1-3 *cis* dimer, in blue. Ca^{2+} presented in green; glycans presented in grey. Model was generated by aligning Pcdh15 EC1-2 from the Pcdh15 EC1-2:Cdh23 EC1-2 complex structure (PDB ID: 4APX) to the Pcdh15 EC1-3 *cis* dimer.

STAR★METHODS

Detailed methods are provided in the online version of this paper and include the following:

- KEY RESOURCES TABLE
- CONTACT FOR REAGENT AND RESOURCE SHARING
- EXPERIMENTAL MODEL AND SUBJECT DETAILS
    - Cell lines
- METHOD DETAILS
    - Plasmids, protein expression and purification
    - Negative-stain EM
    - Crystallization and structure determination Pcdh15 EC 1-3
    - Surface plasmon resonance (SPR)
    - Analytical Ultracentrifugation
    - Cell surface biotinylation and immunoprecipitation experiments
    - Injectoporation and Ca^{2+} imaging
    - Whole mount Immunostaining and Pcdh15 expression level quantification

SUPPLEMENTAL INFORMATION

Supplemental Information includes two tables and eight figures and can be found with this article online at http://dx.doi.org/xxx

CONTACT FOR REAGENT AND RESOURCE SHARING

Further information and requests for resources and reagents should be directed to and will be fulfilled by the Lead Contact, Lawrence Shapiro (lss8@columbia.edu).

EXPERIMENTAL MODEL AND SUBJECT DETAILS

Cell lines

The FreeStyle™ 293F cell line was obtained from Thermo Fisher. The HEK293S GnTI- cells were obtained from ATCC. Human Embryonic Kidney (HEK) 293 cell line, of which the sex is female, is the parental cell for Freestyle™ 293F and HEK293S GnTI- cell lines. HEK293S GnTI- cells are transformed with adenovirus 5 DNA and lack N-acetyl-glucosaminyltransferase I (GnTI) activity, thus rendering them unable to produce complex-type N-glycans. HEK293S GnTI- cells were adapted to suspension culture in Freestyle™ 293 Expression Medium with 2%

FBS at 37 °C. Freestyle™ 293F was obtained from Thermo Fisher and adapted to suspension culture in Freestyle™ 293 Expression Medium at 37 °C.

METHOD DETAILS

Plasmids, protein expression and purification

Our expression vector, pα-H, was a gift from the Laboratory of Daniel Leahy, The University of Texas at Austin. All Pcdh15 fragments were cloned into the pα-H vector. All fragments that started with EC1 use the native signal sequence, while all other fragments use the signal sequence from human BiP. All Pcdh15 fragments and point mutants were expressed by transient transfection of FreeStyle™ 293F cells or GnTI- and initially purified using nickel-affinity with IMAC Sepharose 6 FF Resin (GE Healthcare). All Freestyle™ 293F cell produced fragements were then purified by size exclusion chromatography (Superdex S200 Increase 10/300 GL; GE Healthcare) with buffer containing 150 mM NaCl, 10 mM Tris (pH 8.0), and 3 mM $CaCl_2$. GnTI- produced Pcdh15 EC1-3 was digested with Endogylcosidase H for 24 hours and then purified by size exclusion chromatography (Superdex S200 Increase 10/300 GL; GE Healthcare).

Crystallization and structure determination of the Pcdh15 EC1-3

The Pcdh15 EC1-3 fragment was prepared as described above. Fractions of GNTI-produced, Endoglycosidase H treated Pcdh15 EC1-3 were concentrated to ~10 mg/ml and used for crystallization experiments. Initial crystallization screening was performed with 96 conditions using a Mosquito Crystallization Robot by the vapor diffusion method in sitting drops containing 0.1 µl of protein and 0.1 µl of reservoir solution at 20 °C. Screens were imaged in Formualtrix R1-1000 Imaging Robots. Crystals were picked from a sitting drop from the 96-well

plate screen in a condition of 35% ethylene glycol. Crystals were flash frozen in liquid nitrogen with no additional cryoprotectant.

Diffraction data for were collected with 0.979 Å x-ray at NE-CAT beamline 24-ID-C (Advanced Photon Source, Argonne National Laboratory) and processed with the XDS and AIMLESS. A dataset collected at 1.907 Å was used to calculate a Bijvoet difference Fourier maps to visualize calcium ions. Structures were solved by molecular replacement using PHASER, and iterative model building and refinement were carried out in COOT and PHENIX, respectively. A cross validation (Rfree) test set consisting of 5% of the data was used throughout the refinement processes.

Surface plasmon resonance (SPR)

SPR binding assays were performed using a Biacore T100 biosensor equipped with a Series S CM4 sensor chip. Pcdh15 EC1-3, Pcdh15 EC1-3 D255K, and Pcdh15 EC1-3 K345D were immobilized over independent flow cells using amine-coupling chemistry in HBS pH 7.4 (10 mM HEPES, 150 mM NaCl,) buffer supplemented with 3mM $CaCl_2$, at 25 °C using a flow rate of 20 μL/min. Prior to immobilization the three Pcdh15 EC1-3 variants, which were originally stored in a TRIS buffer, were desalted into HBS pH 7.4/3mM $CaCl_2$ using Zeba spin desalting columns (Thermo Scientific). Dextran surfaces were activated for 7 minutes using equal volumes of 0.1 M NHS (N-Hydroxysuccinimide) and 0.4 M EDC (1-Ethyl-3-(3-dimethylaminopropyl) carbodiimide). Each Pcdh15 EC1-3 protein was immobilized at 37.5 μg/mL in 10 mM sodium acetate, pH 4.0, until the desired immobilization level was achieved. The immobilized surface was blocked using a 4-minute injection of 1.0 M ethanolamine, pH 8.5. Typical immobilization levels ranged between 600-900 RU. An unmodified flow cell served as a reference surface to subtract bulk refractive index changes from the binding signal.

Binding analysis was performed at 25 °C in a running buffer of 10 mM Tris-HCl, pH 8.0, 150 mM NaCl, 3mM $CaCl_2$, 0.5 mg/mL BSA and 0.005% (v/v) Tween-20. Pcdh15 EC1-3 analytes were prepared in running buffer using a three-fold serial dilution ranging between 27 and 3 μM, with the exception of D255K, K345D and K345A mutants which were tested at 27-0.0005 μM using a nine-fold serial dilution. All analyte concentrations were tested in duplicate. During a binding cycle, the association phase between each analyte and the immobilized Pcdh molecule was monitored for 1 minute followed by a two-minute dissociation phase, each at 50 μL/min. At the end of the dissociation phase the signal returned back to baseline thus eliminating the need for a regeneration step. The last step was a buffer wash injection at 100 μL/min for 60 seconds. Every 3 analyte binding cycles, a buffer cycle was introduced to double-reference the binding signals by removing systematic noise and instrument drift. The data was processed using Scrubber 2.0 (BioLogic Software).

Sedimentation Equilibrium Analytical Ultracentrifugation

All AUC experiments were performed using a Beckman XL-A/I analytical ultracentrifuge (Beckman-Coulter, Palo Alto CA, USA), utilizing six-cell centerpieces with straight walls, 12 mm path length, and sapphire windows. All proteins were dialyzed over-night and then diluted in 10 mM Tris, 150 mM NaCl, 3 mM $CaCl_2$, pH 8.0. The samples were diluted to an absorbance at 10 mm and 280 nm of 0.65, 0.43 and 0.23 in channels A, B and C, respectively. Dilution buffer was used as blank. The samples were run at four speeds, the lowest speed held for 20 h then four scans with 1 h interval, the second lowest held for 10 h then four scans with 1h interval, the third lowest and the highest speed were recorded similar the second lowest. Various speeds were used, as detailed in the accompanying Table S2. Measurements were performed at 25 °C, and detection was by UV absorbance at 280 nm. Solvent density and

protein v-bar were determined using the program SednTerp (Alliance Protein Laboratories, Corte Cancion, Thousand Oaks, CA, USA). For calculation of dimeric K_D and apparent molecular weight, all useful data were used in a global fit, using the program HeteroAnalysis, obtained from University of Connecticut. (www.biotech.uconn.edu/auf).

Negative Stain Electron Microscopy

Pcdh15 EC1-11 (10 μg/mL) and Pcdh15 EC1-PICA (20 μg/ml) were applied to 400-mesh carbon-coated copper grids that had been plasma cleaned at 20 mA for 30 seconds using a Gatan Solarus Model 950. The sample was incubated on the grid for 30 seconds and stained with 2% uranyl formate for 30 seconds. Electron micrographs were collected on an FEI Tecnai T20 operating at 120 keV with a magnification of 49,000x, resulting in a pixel size of 3.44 Å. The electron dose was 30 e-/Å2 with an exposure time of 1000 ms. Images were acquired with a Tietz 4k x 4k TemCam-F416 CMOS detector and a defocus of -2.00 μm, using the Leginon software package (Suloway et al., 2005).

Approximately 2,000 particles were manually picked and used to generate 2D templates for use in the FindEM Template Picker, implemented in the Appion package (Lander et al., 2009; Roseman, 2004). The resulting 267,706 particles were subjected to 2D classification using RELION (Kimanius et al., 2016). After 2D classification, 37,133 particles were used for the ab initio reconstruction of eight classes using cryoSPARC (Punjani et al., 2017). One of these classes showed clearly defined EC domains and significant density for most of the protein's expected length, and was subjected to homologous refinement, where C2 symmetry was applied. Resolutions were determined using gold-standard FSC.

Cell surface biotinylation and immunoprecipitation experiments.

Pcdh15-CD2 cDNA (Webb et al., 2011; Xiong et al., 2012) was cloned into the pcDNA3.1 vector with a C-terminal HA tag to increase immunoprecipitation efficiency. LHFPL5 cDNA (Xiong et al. 2012) was cloned to pcDNA3.1 with an N-terminal Myc tag. HEK293 cells on 10 cm culture plates coated with Poly-L-lysine were transfected with 8 μg Pcdh15 plasmid and 2 μg LHFPL5 plasmid using Lipofectamine 3000. 16 hours later, culture plates were transferred onto ice, cells were washed twice with ice cold PBS, and incubated for 30 min on ice with 4 ml PBS containing EZ-Link™Sulfo-NHS-SS-Biotin (1mg/ml). Cells were subsequently washed twice for 5 min with 0.1M Glycine in PBS and twice with PBS. Cells were harvested and lysed in RIPA buffer. Immunoprecipitations were carried out with EZview-Red Anti-HA Affinity beads. Following western blots were carried out with anti-HA antibody, anti-Myc antibody and Transferrin Receptor Antibody. For quantification, western blots from three independent experiments were densitometrically scanned using G-box from Syngene and analyzed with ImageJ. All values are mean ± SEM. One way ANOVA was used to determine statistical significance ($*p < 0.05$, $**p < 0.01$, $***p < 0.001$).

Injectoporation and Ca^{2+} imaging.

Injectoporation experiments were carried out essentially as described (Xiong et al., 2012; Xiong et al., 2014; Zhao et al., 2014). In brief, the organ of Corti was isolated from *Pcdh15*-deficient *Ames-waltzer*^{av3J} mice (Alagramam et al., 2001) and cultured in DMEM/F12 with 1.5 μg/ml ampicillin. For electroporation, glass electrodes (2 μm diameter) were used to deliver plasmid (500 ng/μl in 1x HBSS) to the sensory epithelium. A series of 3 pulses was applied at 1 sec intervals with a magnitude of 60V and duration of 15 msec (ECM 830 square wave electroporator; BTX). We used G-CaMP3 for Ca^{2+} imaging. Imaging was carried out on an upright Olympus BX51WI microscope mounted with a 60x water-immersion objective and

Qimaging ROLERA-QX camera, controlled by Micro-Manager 1.3 software (Edelstein et al., 2010). Hair bundles were stimulated with a fluid jet that was applied through a glass electrode (2 μm tip-diameter), which was filled with bath solution. Stimuli were applied using Patchmaster 2.35 software (HEKA) and 20 psi air pressure (Picospritzer III microinjector). Images were collected with a 2 sec sampling rate. A series of fluid-jet stimulations (0.1, 0.3, 0.5 sec) was applied (60 sec intervals). Responses induced by 0.3 sec fluid-jet stimulation were used for quantitative analysis. Data analysis was performed using Excel (Microsoft) and Igor pro 6 (WaveMetrics, Lake Oswego, OR). Calcium signal ($\Delta F/F$) was calculated with the equation: $(F-F_0)/F_0$, where F_0 is the averaged fluorescence baseline at the beginning. All data are mean ± SEM. Student's two-tailed unpaired t test was used to determine statistical significance ($*p < 0.05$, $**p < 0.01$, $***p < 0.001$)

Plasmids used for injectoporation were as follows: (i) CMV-GCaMP3 has been described previously (Xiong et al., 2012; Xiong et al., 2014); (ii) CMV-Pcdh15-CD2 (Webb et al., 2011; Xiong et al., 2012) was used to express wild-type Pcdh15 in hair cells. All Pcdh15 point mutations were generated using the QuikChange II XL site-directed mutagenesis Kit from Agilent.

Whole mount Immunostaining and Pcdh15 expression level quantification.

Whole mount staining was carried out as described (Zhao et al., 2014). Stereocilia were visualized by phalloidin staining, and Pcdh15 was evaluated with antibodies to Pcdh15-CD2 (Webb et al., 2011). Additional reagents were Alexa Fluor 488- goat anti-rabbit, Alexa Fluor 555 phalloidin (Invitrogen, Carlsbad, CA). Immunostaining imaging were obtained with Deltavision Imaging System (GE Healthcare Life Sciences).

For a quantitative assessment of Pcdh15 expression levels, we used Imaris 9.1(Oxford Instruments) to generate 3D reconstructions of hair bundles. We calculated the fluorescence volume of Pcdh15 and phalloidin, and used the volume ratio to determine relative Pcdh15 expression level between wild-type and mutant constructs from 11-45 hair cells. All data are mean ± SEM. Student's two-tailed unpaired t test was used to determine statistical significance ($*p < 0.05$, $**p < 0.01$, $***p < 0.001$).

DATA AND SOFTWARE AVAILABILITY

Coordinates and structural factors for Pcdh15 EC1-3 Dimer are available from the Protein Data Bank under accession code PDB 6CV7.

STAR★METHODS

Detailed methods are provided in the online version of this paper and include the following:

- KEY RESOURCES TABLE
- CONTACT FOR REAGENT AND RESOURCE SHARING
- EXPERIMENTAL MODEL AND SUBJECT DETAILS
  - Cell lines
- METHOD DETAILS
  - Plasmids, protein expression and purification
  - Negative-stain EM
  - Crystallization and structure determination Pcdh15 EC 1-3
  - Surface plasmon resonance (SPR)
  - Analytical Ultracentrifugation
  - Cell surface biotinylation and immunoprecipitation experiments
  - Injectoporation and Ca^{2+} imaging
  - Whole mount Immunostaining and Pcdh15 expression level quantification

SUPPLEMENTAL INFORMATION

Supplemental Information includes two tables and eight figures and can be found with this article online at http://dx.doi.org/xxx

Author contributions

G.D., X.Q., C.S.P., B.C., B.H., U.M. and L.S. designed experiments and analyzed data; M.A.R. performed electron microscopy experiments; X.Q. carried out functional studies in hair cells; X.L. analyzed Pcdh15 expression in heterologous cells; B.Z. and G. P. cloned Pcdh15 expression constructs. P.S.K. performed SPR experiments; G.A. performed analytical ultracentrifugation experiments; R.R. performed sequence alignments; G.D. produced proteins and performed crystallography experiments. G.D., U.M. and L.S. wrote the paper.

Acknowledgements

We thank Surajit Banerjee and Igor Kourinov for help with synchrotron data collection conducted at the APS NE-CAT 24-ID-C beamline, which is supported by National Institutes of Health (NIH) P41 GM103403. We acknowledge the support of a National Science Foundation grant (MCB-1412472) to B.H., and a joint NIH grant (R01DC016960) to U.M. and L.S. G.D. was supported by an NIH training grant. The computing in this project was supported by two NIH instrumentation grants (S10OD012351 and S10OD021764) received by the Department of Systems Biology at Columbia University. Electron microscopy was performed at the Simons Electron Microscopy Center and National Resource for Automated Molecular Microscopy located at the New York Structural Biology Center, supported by grants from the Simons Foundation (349247), NYSTAR, and the NIH National Institute of General Medical Sciences

(GM103310) with additional support from Agouron Institute (Grant Number: F00316) and NIH S10 OD019994-01.

STAR★METHODS

KEY RESOURCES TABLE

REAGENT or RESOURCE	SOURCE	IDENTIFIER
Chemicals, Peptides, Recombinant Proteins, Antibodies and Biosensors		
Pcdh15 fragments and point mutants	This paper	N/A
Pcdh15-CD2	(Webb et al., 2011), This paper	N/A
G-CaMP3	Addgene	Cat#22692
Myc-LHFPL5	This paper	N/A
Rabbit anti-Pcdh15-CD2 antibody	(Webb et al., 2011)	N/A
Alexa Fluor™ 488- goat anti-rabbit	Invitrogen	Cat# A11070
Alexa Fluor™ 555 Phalloidin	Invitrogen	Cat# A34055
Triton X-100	Sigma	Cat# T8532
DMEM/F12	Gibco	Cat# 11330-057
DMEM/F12, no phenol red	Gibco	Cat# 21041-025
HBSS	Gibco	Cat# 14175095
FBS	Gemini	Cat# 100–106
Tris Base	Fisher Scientific	Cat# BP152-5
Sodium Chloride	Fisher Scientific	Cat# S271-10
Calcium Chloride Dihydrate	JT Baker	Cat# 1336-01
Imidazole	ACROS	Cat# 301870025
Endoglycosidase HF	New England Biolabs	Cat# P0703S
Ethylene Glycol	Fluka	Cat# 03760
HEPES	Sigma	Cat# H3375
Polyethylenimine	Polysciences	Cat# 24765-2
N-Hydroxysuccinimide	Thermo Fisher Scientific	Cat# 24500
1-Ethyl-3-(3-dimethylaminopropyl) carbodiimide	Thermo Fisher Scientific	Cat# 22980
Sodium Acetate	Sigma	Cat# S7545
Ethanolamine	Sigma	Cat# 398136
Tween-20	Sigma	Cat# P7949
BSA	Sigma	Cat# A7906
Uranyl Formate	Electron Microscopy Sciences	Cat# 22451
Freestyle™ 293 Expression Media	Thermo Fisher Scientific	Cat# 12338-018
Opti-MEM™ Reduced Serum Media	Thermo Fisher Scientific	Cat# 31985-070
CM4 chip	GE Healthcare	Cat# BR100534
Poly-L-lysine	Sigma	Cat# P2636
Lipofectamine 3000	ThermoFisher Scientific	Cat# L3000015
EZ-Link™Sulfo-NHS-SS-Biotin	ThermoFisher Scientific	Cat# 21217
EZview-Red Anti-HA Affinity beads	Sigma	Cat# E6779
anti-HA antibody	Cell Signaling Technology	Cat# 2367S
anti-Myc antibody	Cell Signaling Technology	Cat# 2276S

Transferrin Receptor Antibody	Invitrogen	Cat# 13-6800
Glycine	Sigma	Cat# G7126-5KG
Critical Commercial Assays		
Spin Miniprep Kit	Qiagen	Cat# 27106
Hispeed Plasmid Maxi Kit	Qiagen	Cat# 12663
QuikChange II XL site-directed mutagenesis Kit	Agilent	Cat # 200521
Deposited Data		
Crystal structure of mouse Pcdh15 EC1-3	This paper	PDB ID: 6CV7
Experimental Models: Cell Lines and mice		
Human: FreeStyle™ 293-F cells	Thermo Fisher Scientific	Cat# R79007
Human: HEK293S GnTI- Cells	ATCC	Cat# CRL-3022
HEK293 cells	ATCC	Cat# CRL-1573
Ames-waltzer^{av3J} mice	The Jackson Laboratory	Cat# 002072
Recombinant DNA		
pα-H vector	Laboratory of Daniel Leahy	N/A
Software and Algorithms		
XDS	(Kabsch, 2010)	http://xds.mpimf-heidelberg.mpg.de
AIMLESS	(Evans and Murshudov, 2013)	http://www.ccp4.ac.uk
Phenix	(Adams et al., 2004)	http://www.hkl-xray.com/
Coot	(Emsley and Cowtan, 2004)	https://www2.mrc-lmb.cam.ac.uk/personal/pemsley/coot/
Pymol	Schrödinger	https://pymol.org
PDBePISA	(Krissinel and Henrick, 2007)	http://www.ebi.ac.uk/pdbe/pisa/
Scrubber 2.0	BioLogic Software	http://www.biologic.com.au
SednTerp	Dr. Thomas Laue	http://bitcwiki.sr.unh.edu/index.php/Main_Page
HeteroAnalysis	(Cole and Lary)	https://core.uconn.edu/auf
FindEm	(Roseman, 2004)	http://emg.nysbc.org/redmine/projects/appion/wiki/Appion_Home
Appion	(Lander et al., 2009)	http://emg.nysbc.org/redmine/projects/appion/wiki/Appion_Home
RELION	(Kimanius et al., 2016)	https://www2.mrc-lmb.cam.ac.uk/relion/index.php?title=Main_Page
cryoSPARC	(Punjani et al., 2017)	https://cryosparc.com
Patchmaster 2.35	HEKA	http://www.heka.com/downloads/downloads_main.html
Micro-Manager 1.4 software.	(Edelstein et al., 2010)	https://micro-manager.org/wiki/
Igor pro 6	WaveMetrics	https://www.wavemetrics.com/
Imaris 9.1	Oxford Instruments	http://www.bitplane.com/imaris
Image J	NIH	https://imagej.nih.gov/ij/

CONTACT FOR REAGENT AND RESOURCE SHARING

Further information and requests for resources and reagents should be directed to and will be fulfilled by the Lead Contact, Lawrence Shapiro (lss8@columbia.edu).

EXPERIMENTAL MODEL AND SUBJECT DETAILS

Cell lines

The FreeStyle™ 293F cell line was obtained from Thermo Fisher. The HEK293S GnTI- cells were obtained from ATCC. Human Embryonic Kidney (HEK) 293 cell line, of which the sex is female, is the parental cell for Freestyle™ 293F and HEK293S GnTI- cell lines. HEK293S GnTI- cells are transformed with adenovirus 5 DNA and lack N-acetyl-glucosaminyltransferase I (GnTI) activity, thus rendering them unable to produce complex-type N-glycans. HEK293S GnTI- cells were adapted to suspension culture in Freestyle™ 293 Expression Medium with 2% FBS at 37 °C. Freestyle™ 293F was obtained from Thermo Fisher and adapted to suspension culture in Freestyle™ 293 Expression Medium at 37 °C.

METHOD DETAILS

Plasmids, protein expression and purification

Our expression vector, pα-H, was a gift from the Laboratory of Daniel Leahy, The University of Texas at Austin. All Pcdh15 fragments were cloned into the pα-H vector. All fragments that started with EC1 use the native signal sequence, while all other fragments use the signal sequence from human BiP. All Pcdh15 fragments and point mutants were expressed by transient transfection of FreeStyle™ 293F cells or GnTI- and initially purified using nickel-affinity with IMAC Sepharose 6 FF Resin (GE Healthcare). All Freestyle™ 293F cell produced fragements

were then purified by size exclusion chromatography (Superdex S200 Increase 10/300 GL; GE Healthcare) with buffer containing 150 mM NaCl, 10 mM Tris (pH 8.0), and 3 mM $CaCl_2$. GnTI- produced Pcdh15 EC1-3 was digested with Endogylcosidase H for 24 hours and then purified by size exclusion chromatography (Superdex S200 Increase 10/300 GL; GE Healthcare).

Crystallization and structure determination of the Pcdh15 EC1-3

The Pcdh15 EC1-3 fragment was prepared as described above. Fractions of GNTI-produced, Endoglycosidase H treated Pcdh15 EC1-3 were concentrated to ~10 mg/ml and used for crystallization experiments. Initial crystallization screening was performed with 96 conditions using a Mosquito Crystallization Robot by the vapor diffusion method in sitting drops containing 0.1 µl of protein and 0.1 µl of reservoir solution at 20 °C. Screens were imaged in Formualtrix R1-1000 Imaging Robots. Crystals were picked from a sitting drop from the 96-well plate screen in a condition of 35% ethylene glycol. Crystals were flash frozen in liquid nitrogen with no additional cryoprotectant.

Diffraction data for were collected with 0.979 Å x-ray at NE-CAT beamline 24-ID-C (Advanced Photon Source, Argonne National Laboratory) and processed with the XDS and AIMLESS. A dataset collected at 1.907 Å was used to calculate a Bijvoet difference Fourier maps to visualize calcium ions. Structures were solved by molecular replacement using PHASER, and iterative model building and refinement were carried out in COOT and PHENIX, respectively. A cross validation (Rfree) test set consisting of 5% of the data was used throughout the refinement processes.

Surface plasmon resonance (SPR)

SPR binding assays were performed using a Biacore T100 biosensor equipped with a Series S CM4 sensor chip. Pcdh15 EC1-3, Pcdh15 EC1-3 D255K, and Pcdh15 EC1-3 K345D

were immobilized over independent flow cells using amine-coupling chemistry in HBS pH 7.4 (10 mM HEPES, 150 mM NaCl,) buffer supplemented with 3mM $CaCl_2$, at 25 °C using a flow rate of 20 μL/min. Prior to immobilization the three Pcdh15 EC1-3 variants, which were originally stored in a TRIS buffer, were desalted into HBS pH 7.4/3mM $CaCl_2$ using Zeba spin desalting columns (Thermo Scientific). Dextran surfaces were activated for 7 minutes using equal volumes of 0.1 M NHS (N-Hydroxysuccinimide) and 0.4 M EDC (1-Ethyl-3-(3-dimethylaminopropyl) carbodiimide). Each Pcdh15 EC1-3 protein was immobilized at 37.5 μg/mL in 10 mM sodium acetate, pH 4.0, until the desired immobilization level was achieved. The immobilized surface was blocked using a 4-minute injection of 1.0 M ethanolamine, pH 8.5. Typical immobilization levels ranged between 600-900 RU. An unmodified flow cell served as a reference surface to subtract bulk refractive index changes from the binding signal.

Binding analysis was performed at 25 °C in a running buffer of 10 mM Tris-HCl, pH 8.0, 150 mM NaCl, 3mM $CaCl_2$, 0.5 mg/mL BSA and 0.005% (v/v) Tween-20. Pcdh15 EC1-3 analytes were prepared in running buffer using a three-fold serial dilution ranging between 27 and 3 μM, with the exception of D255K, K345D and K345A mutants which were tested at 27-0.0005 μM using a nine-fold serial dilution. All analyte concentrations were tested in duplicate. During a binding cycle, the association phase between each analyte and the immobilized Pcdh molecule was monitored for 1 minute followed by a two-minute dissociation phase, each at 50 μL/min. At the end of the dissociation phase the signal returned back to baseline thus eliminating the need for a regeneration step. The last step was a buffer wash injection at 100 μL/min for 60 seconds. Every 3 analyte binding cycles, a buffer cycle was introduced to double-reference the binding signals by removing systematic noise and instrument drift. The data was processed using Scrubber 2.0 (BioLogic Software).

Sedimentation Equilibrium Analytical Ultracentrifugation

All AUC experiments were performed using a Beckman XL-A/I analytical ultracentrifuge (Beckman-Coulter, Palo Alto CA, USA), utilizing six-cell centerpieces with straight walls, 12 mm path length, and sapphire windows. All proteins were dialyzed over-night and then diluted in 10 mM Tris, 150 mM NaCl, 3 mM $CaCl_2$, pH 8.0. The samples were diluted to an absorbance at 10 mm and 280 nm of 0.65, 0.43 and 0.23 in channels A, B and C, respectively. Dilution buffer was used as blank. The samples were run at four speeds, the lowest speed held for 20 h then four scans with 1 h interval, the second lowest held for 10 h then four scans with 1h interval, the third lowest and the highest speed were recorded similar the second lowest. Various speeds were used, as detailed in the accompanying Table S2. Measurements were performed at 25 °C, and detection was by UV absorbance at 280 nm. Solvent density and protein v-bar were determined using the program SednTerp (Alliance Protein Laboratories, Corte Cancion, Thousand Oaks, CA, USA). For calculation of dimeric K_D and apparent molecular weight, all useful data were used in a global fit, using the program HeteroAnalysis, obtained from University of Connecticut. (www.biotech.uconn.edu/auf).

Negative Stain Electron Microscopy

Pcdh15 EC1-11 (10 μg/mL) and Pcdh15 EC1-PICA (20 μg/ml) were applied to 400-mesh carbon-coated copper grids that had been plasma cleaned at 20 mA for 30 seconds using a Gatan Solarus Model 950. The sample was incubated on the grid for 30 seconds and stained with 2% uranyl formate for 30 seconds. Electron micrographs were collected on an FEI Tecnai T20 operating at 120 keV with a magnification of 49,000x, resulting in a pixel size of 3.44 Å. The electron dose was 30 e-/Å2 with an exposure time of 1000 ms. Images were acquired with a

Tietz 4k x 4k TemCam-F416 CMOS detector and a defocus of -2.00 μm, using the Leginon software package (Suloway et al., 2005).

Approximately 2,000 particles were manually picked and used to generate 2D templates for use in the FindEM Template Picker, implemented in the Appion package (Lander et al., 2009; Roseman, 2004). The resulting 267,706 particles were subjected to 2D classification using RELION (Kimanius et al., 2016). After 2D classification, 37,133 particles were used for the ab initio reconstruction of eight classes using cryoSPARC (Punjani et al., 2017). One of these classes showed clearly defined EC domains and significant density for most of the protein's expected length, and was subjected to homologous refinement, where C2 symmetry was applied. Resolutions were determined using gold-standard FSC.

Cell surface biotinylation and immunoprecipitation experiments.

Pcdh15-CD2 cDNA (Webb et al., 2011; Xiong et al., 2012) was cloned into the pcDNA3.1 vector with a C-terminal HA tag to increase immunoprecipitation efficiency. LHFPL5 cDNA (Xiong et al. 2012) was cloned to pcDNA3.1 with an N-terminal Myc tag. HEK293 cells on 10 cm culture plates coated with Poly-L-lysine were transfected with 8 μg Pcdh15 plasmid and 2 μg LHFPL5 plasmid using Lipofectamine 3000. 16 hours later, culture plates were transferred onto ice, cells were washed twice with ice cold PBS, and incubated for 30 min on ice with 4 ml PBS containing EZ-Link™Sulfo-NHS-SS-Biotin (1mg/ml). Cells were subsequently washed twice for 5 min with 0.1M Glycine in PBS and twice with PBS. Cells were harvested and lysed in RIPA buffer. Immunoprecipitations were carried out with EZview-Red Anti-HA Affinity beads. Following western blots were carried out with anti-HA antibody, anti-Myc antibody and Transferrin Receptor Antibody. For quantification, western blots from three independent experiments were densitometrically scanned using G-box from Syngene and analyzed with

ImageJ. All values are mean ± SEM. One way ANOVA was used to determine statistical significance (∗p < 0.05, ∗∗p < 0.01, ∗∗∗p < 0.001).

Injectoporation and Ca^{2+} imaging.

Injectoporation experiments were carried out essentially as described (Xiong et al., 2012; Xiong et al., 2014; Zhao et al., 2014). In brief, the organ of Corti was isolated from *Pcdh15*-deficient *Ames-waltzer*^{av3J} mice (Alagramam et al., 2001) and cultured in DMEM/F12 with 1.5 μg/ml ampicillin. For electroporation, glass electrodes (2 μm diameter) were used to deliver plasmid (500 ng/μl in 1x HBSS) to the sensory epithelium. A series of 3 pulses was applied at 1 sec intervals with a magnitude of 60V and duration of 15 msec (ECM 830 square wave electroporator; BTX). We used G-CaMP3 for Ca^{2+} imaging. Imaging was carried out on an upright Olympus BX51WI microscope mounted with a 60x water-immersion objective and Qimaging ROLERA-QX camera, controlled by Micro-Manager 1.3 software (Edelstein et al., 2010)**.** Hair bundles were stimulated with a fluid jet that was applied through a glass electrode (2 μm tip-diameter), which was filled with bath solution. Stimuli were applied using Patchmaster 2.35 software (HEKA) and 20 psi air pressure (Picospritzer III microinjector). Images were collected with a 2 sec sampling rate. A series of fluid-jet stimulations (0.1, 0.3, 0.5 sec) was applied (60 sec intervals). Responses induced by 0.3 sec fluid-jet stimulation were used for quantitative analysis. Data analysis was performed using Excel (Microsoft) and Igor pro 6 (WaveMetrics, Lake Oswego, OR). Calcium signal (ΔF/F) was calculated with the equation: $(F-F_0)/F_0$, where F_0 is the averaged fluorescence baseline at the beginning. All data are mean ± SEM. Student's two-tailed unpaired t test was used to determine statistical significance (∗p < 0.05, ∗∗p < 0.01, ∗∗∗p < 0.001)

Plasmids used for injectoporation were as follows: (i) CMV-GCaMP3 has been described previously (Xiong et al., 2012; Xiong et al., 2014); (ii) CMV-Pcdh15-CD2 (Webb et al., 2011; Xiong et al., 2012) was used to express wild-type Pcdh15 in hair cells. All Pcdh15 point mutations were generated using the QuikChange II XL site-directed mutagenesis Kit from Agilent.

Whole mount Immunostaining and Pcdh15 expression level quantification.

Whole mount staining was carried out as described (Zhao et al., 2014). Stereocilia were visualized by phalloidin staining, and Pcdh15 was evaluated with antibodies to Pcdh15-CD2 (Webb et al., 2011). Additional reagents were Alexa Fluor 488- goat anti-rabbit, Alexa Fluor 555 phalloidin (Invitrogen, Carlsbad, CA). Immunostaining imaging were obtained with Deltavision Imaging System (GE Healthcare Life Sciences).

For a quantitative assessment of Pcdh15 expression levels, we used Imaris 9.1(Oxford Instruments) to generate 3D reconstructions of hair bundles. We calculated the fluorescence volume of Pcdh15 and phalloidin, and used the volume ratio to determine relative Pcdh15 expression level between wild-type and mutant constructs from 11-45 hair cells. All data are mean ± SEM. Student's two-tailed unpaired t test was used to determine statistical significance ($*p < 0.05$, $**p < 0.01$, $***p < 0.001$).

DATA AND SOFTWARE AVAILABILITY

Coordinates and structural factors for Pcdh15 EC1-3 Dimer are available from the Protein Data Bank under accession code PDB 6CV7.

Declaration of Interests

The authors declare no competing interests.

Figure 1

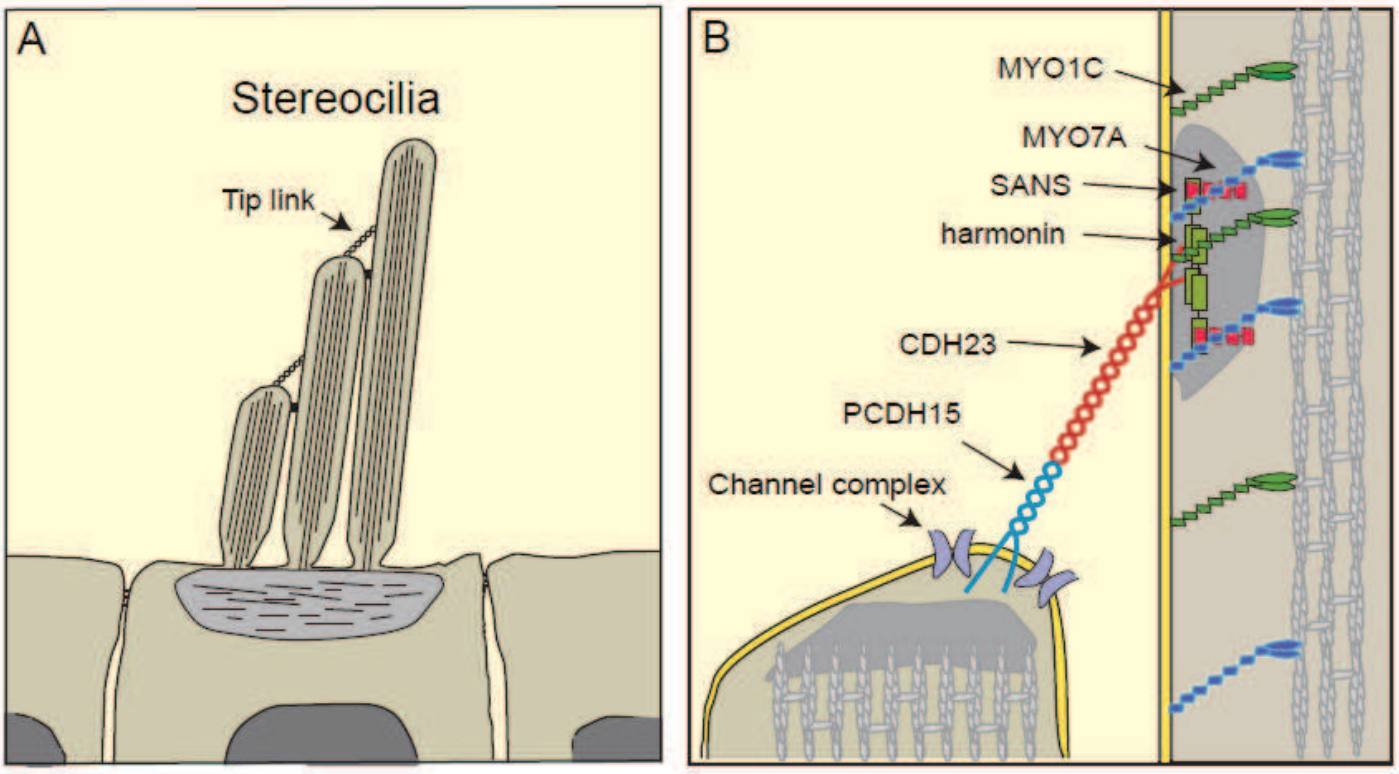
A
Stereocilia
Tip link
B
MYO1C
MYO7A
SANS
harmonin
CDH23
PCDH15
Channel complex

Figure 2

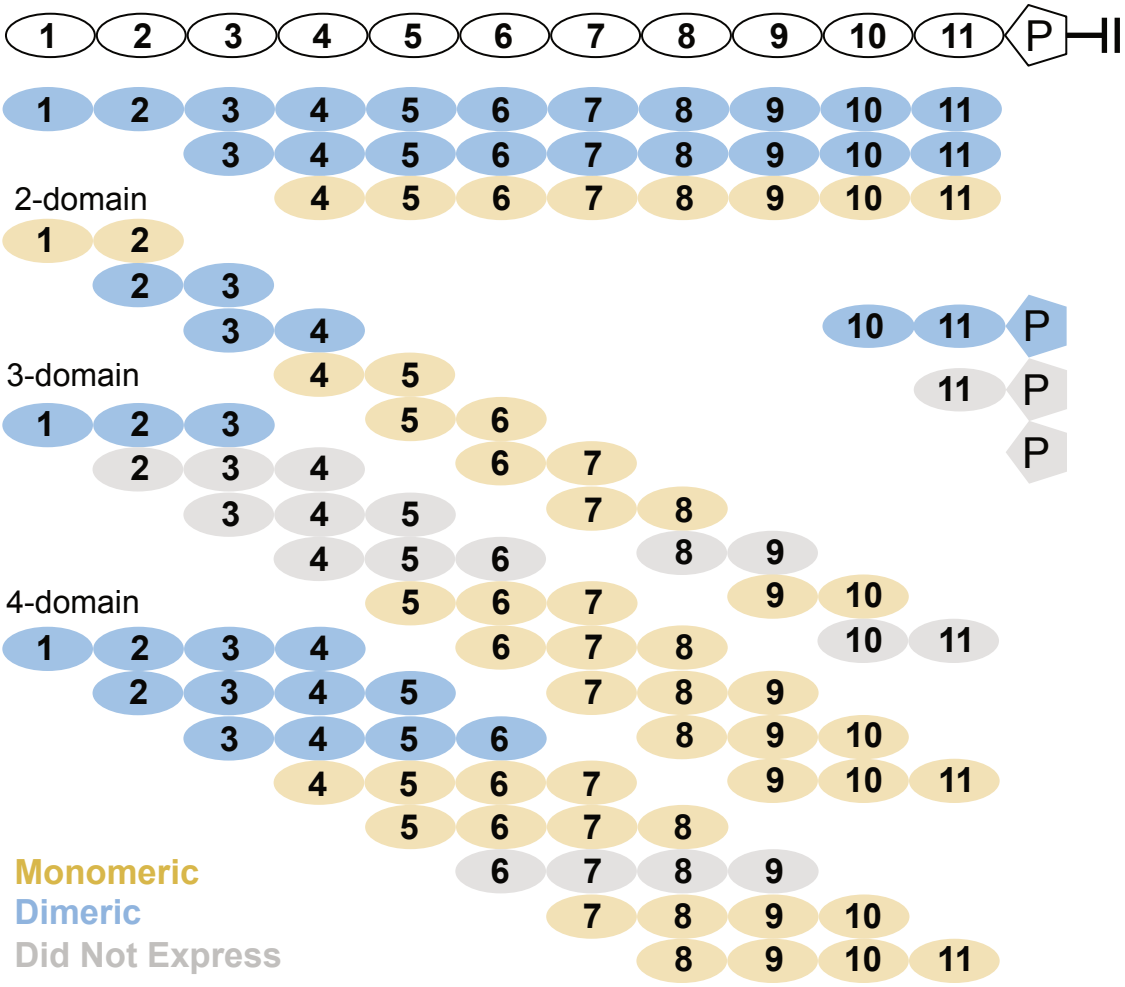
1 2 3 4 5 6 7 8 9 10 11 P
2-domain
3-domain
4-domain
Monomeric
Dimeric
Did Not Express

Figure 3

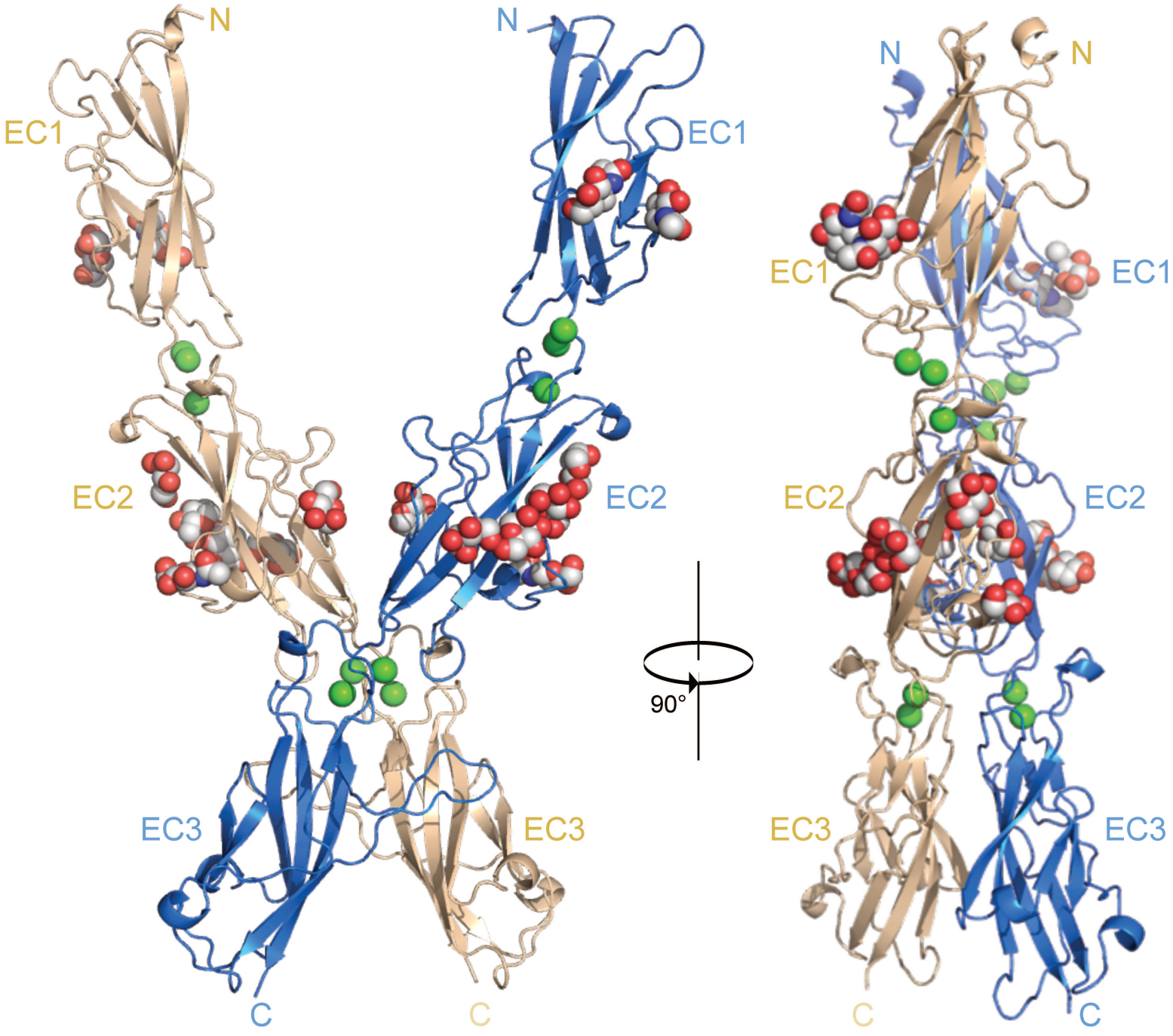

Figure 4

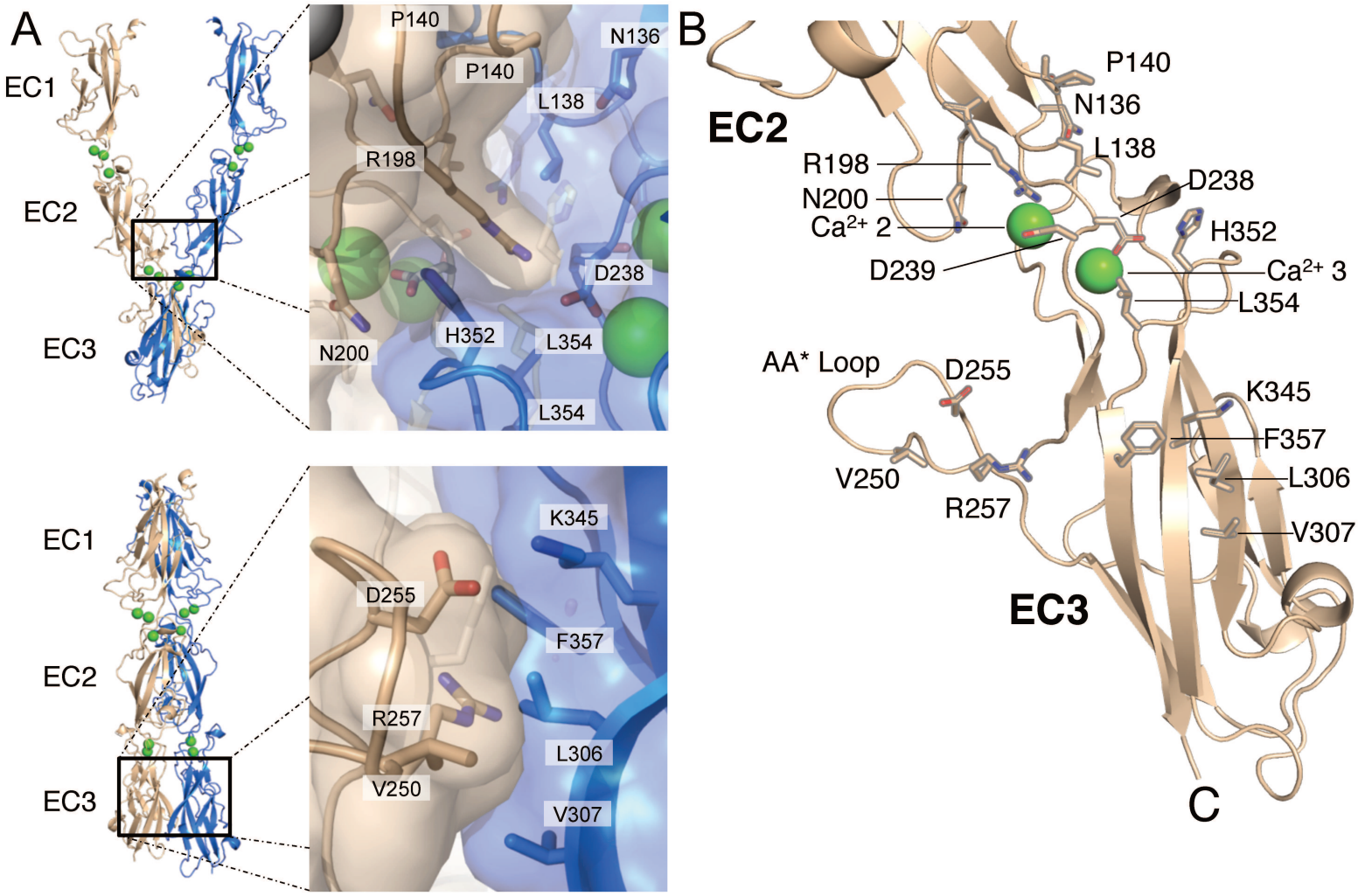
A
EC1
EC2
EC3
P140
N136
P140
L138
R198
D238
H352
N200
L354
L354
EC1
EC2
EC3
K345
D255
F357
R257
L306
V250
V307
B
EC2
P140
N136
L138
R198
D238
N200
Ca2+ 2
H352
D239
Ca2+ 3
L354
AA* Loop
D255
K345
F357
V250
L306
R257
V307
EC3
C

Figure 5

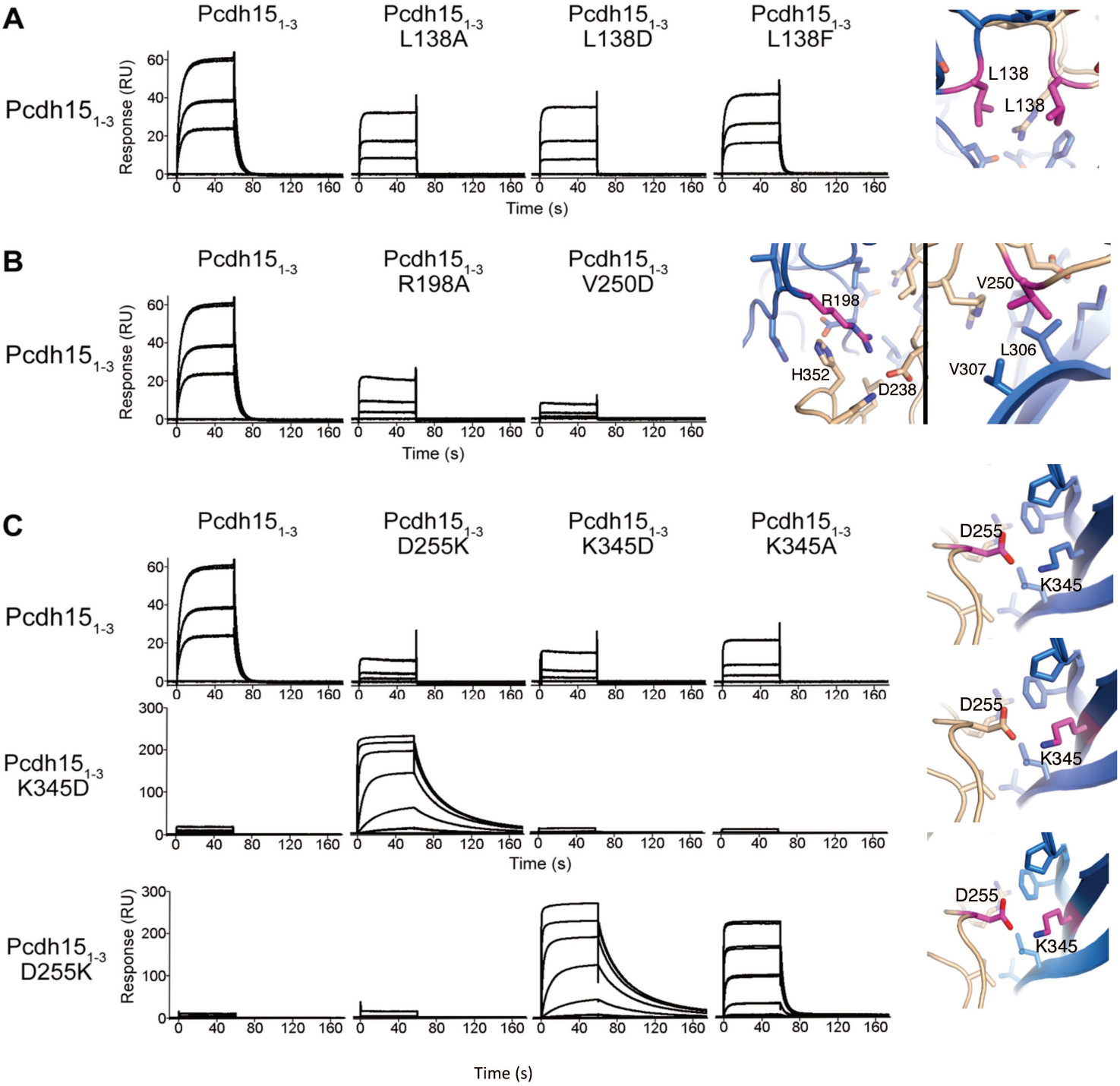
A
Pcdh15 1-3
Pcdh15 1-3 L138A
Pcdh15 1-3 L138D
Pcdh15 1-3 L138F
Pcdh15 1-3
Response (RU)
Time (s)
L138
L138
B
Pcdh15 1-3
Pcdh15 1-3 R198A
Pcdh15 1-3 V250D
Pcdh15 1-3
Response (RU)
Time (s)
R198
H352
D238
V250
L306
V307
C
Pcdh15 1-3
Pcdh15 1-3 D255K
Pcdh15 1-3 K345D
Pcdh15 1-3 K345A
Pcdh15 1-3
Pcdh15 1-3 K345D
Pcdh15 1-3 D255K
Response (RU)
Time (s)
D255
K345
D255
K345
D255
K345

Figure 6

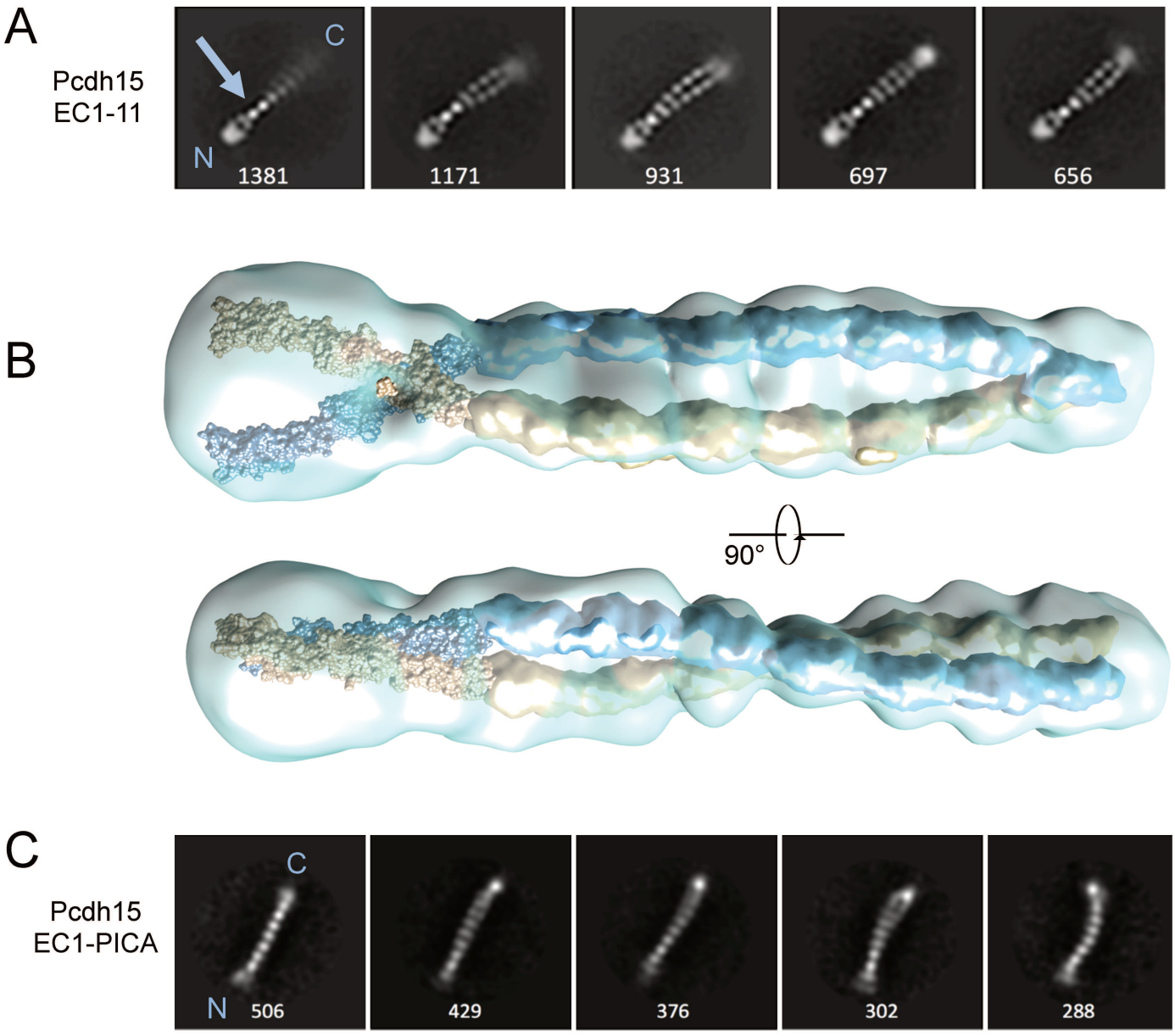
A
Pcdh15
EC1-11
C
N
1381
1171
931
697
656
B
90°
C
Pcdh15
EC1-PICA
N
506
429
376
302
288

Figure 7

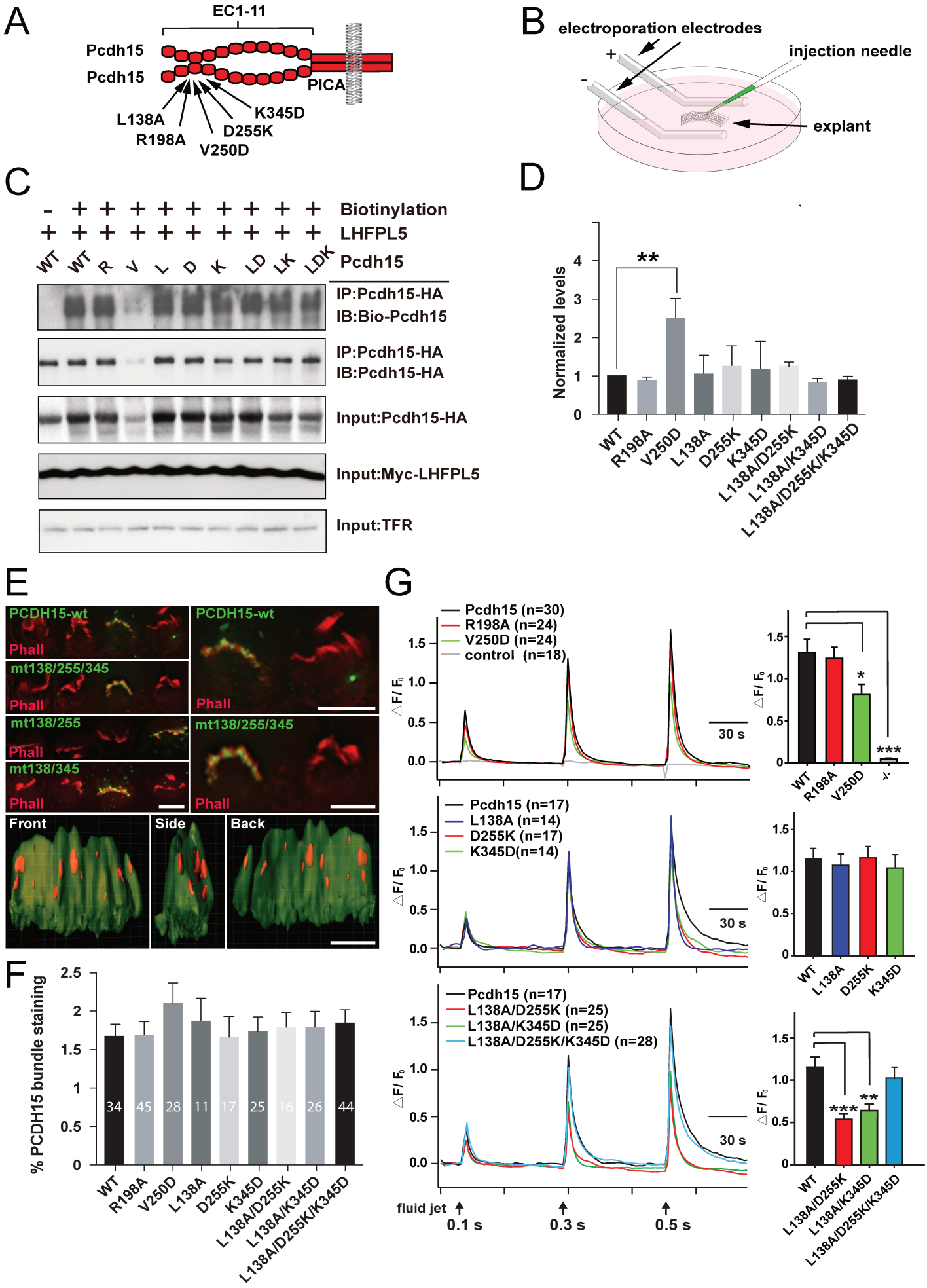
A
EC1-11
Pcdh15
Pcdh15
PICA
L138A
R198A
V250D
D255K
K345D
B
electroporation electrodes
injection needle
explant
C
Biotinylation
LHFPL5
WT WT R V L D K LD LK LDK
Pcdh15
IP:Pcdh15-HA
IB:Bio-Pcdh15
IP:Pcdh15-HA
IB:Pcdh15-HA
Input:Pcdh15-HA
Input:Myc-LHFPL5
Input:TFR
D
Normalized levels
**
WT
R198A
V250D
L138A
D255K
K345D
L138A/D255K
L138A/K345D
L138A/D255K/K345D
E
PCDH15-wt
PhalI
mt138/255/345
mt138/255
mt138/345
Front
Side
Back
F
% PCDH15 bundle staining
34 45 28 11 17 25 16 26 44
G
Pcdh15 (n=30)
R198A (n=24)
V250D (n=24)
control (n=18)
Pcdh15 (n=17)
L138A (n=14)
D255K (n=17)
K345D(n=14)
Pcdh15 (n=17)
L138A/D255K (n=25)
L138A/K345D (n=25)
L138A/D255K/K345D (n=28)
△F/ F0
30 s
fluid jet
0.1 s
0.3 s
0.5 s

Figure 8

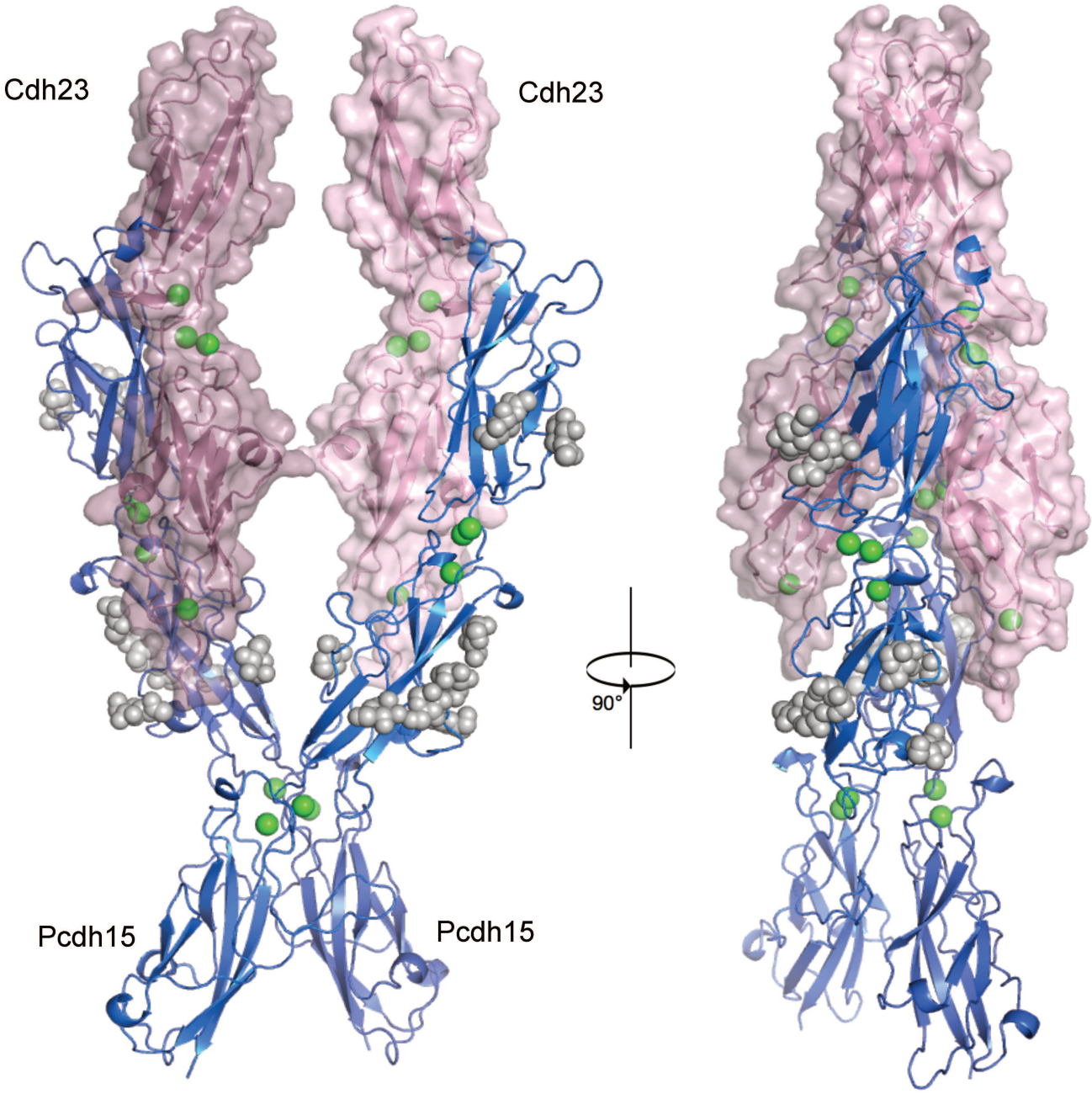

Table S1

Pcdh15 EC1-3	
Wavelength (Å)	0.979 Å
Resolution range (Å)	99.11 - 1.692 (1.753 - 1.692)
Space group	P 65 2 2
Unit cell	114.444 114.444 172.011 90 90 120
Total reflections	1345148 (45588)
Unique reflections	73884 (6959)
Multiplicity	18.2 (6.6)
Completeness (%)	99.26 (92.50)
Mean I/sigma(I)	20.19 (0.69)
Wilson B-factor	29.23
R-merge	0.1154 (1.97)
R-meas	0.1186
CC1/2	0.992 (0.362)
CC*	0.998 (0.729)
Reflections used for R-free	
R-work	0.1630 (0.3748)
R-free	0.1946 (0.729)
Number of non-hydrogen atoms	3620
macromolecules	2988
ligands	126
water	506
Protein residues	366
RMS(bonds)	0.017
RMS(angles)	1.65
Ramachandran favored (%)	1.00E+02
Ramachandran allowed (%)	0
Ramachandran outliers (%)	0
Clashscore	4.82
Average B-factor	35.7
macromolecules	33.9
ligands	40.8
solvent	44.9

Table S1. Crystallography Statistics for Pcdh15 EC1-3, Related to Figure 3

Speeds, rpm	Construct	K_D (μM)
15000, 19000, 23000, 27000	EC 1-2 WT	Monomer
	EC 2-3 WT	18.1 ± 0.4
	EC 3-4 WT	120.0 ± 7.2
	EC 4-5 WT	Monomer
	EC 5-6 WT	Monomer
	EC 6-7 WT	Monomer
	EC 7-8 WT	208 ± 10.7
	EC 9-10 WT	Monomer
	EC 5-7 WT	Monomer
	EC 6-8 WT	Monomer
	EC 7-9 WT	Monomer
	EC 8-10 WT	Monomer
	EC 9-11 WT	Monomer
	EC 1-3 K345A	Monomer
	EC 1-3 K345D	Monomer
	EC 1-3 D255K	Monomer
	EC 1-3 L138D	Monomer
	EC 1-3 L138A	Monomer
	EC 1-3 L138F	15.3 ± 3.1
11000, 14000, 17000, 20000	EC 1-4 WT	Dimer (MALS)
	EC 2-5 WT	Dimer (MALS)
	EC 3-6 WT	Dimer (MALS)
	EC 4-7 WT	Monomer
	EC 5-8 WT	Monomer
	EC 7-10 WT	Monomer
	EC 8-11 WT	Monomer
9000, 11000, 13000, 15000	EC 1-3 WT	1.2 ± 0.5
	EC 1-3 R198A	Monomer
	EC 1-3 V250D	Monomer
	EC 3-11 WT	220.0 ± 78
	EC 4-11 WT	Monomer
	EC 5-11 WT	Monomer
7000, 9000, 11000, 13000	EC 1-11 WT	0.2 ± 0.1
	EC 1-11 R198A	21.0 ± 3.4
	EC 1-11 V250D	Monomer
	EC 3-11 WT	220.0 ± 78

Table S2. Rotor Speeds and K_Ds for various Pcdh15 protein fragments in AUC experiments, Related to Figure 2

Figure S1

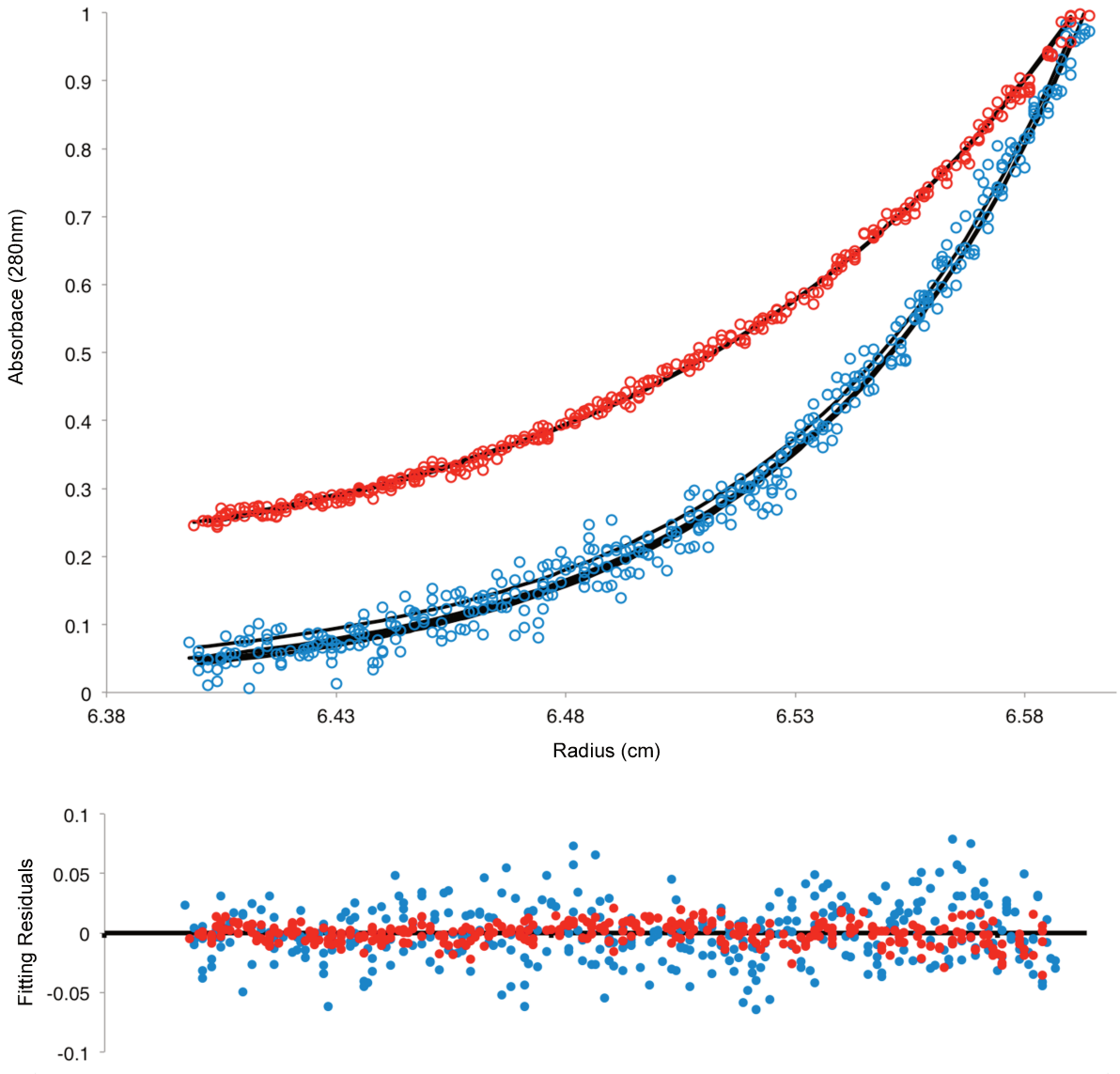

Figure S1. Sample Sedimentation Equilibrium traces for Wild-type and Mutant Pcdh15 EC1-3, Related to Figure 2
Purified wild-type Pcdh15 EC1-3, raw data plotted in blue, and Pcdh15 EC1-3 V250D, raw data plotted in red, were loaded at concentrations of 0.58 mg/ml and analyzed by sedimentation equilibrium analytical ultracentrifucation, with a rotor speed of 15000 rpm. Non-linear fits for a monomer-to-dimer model are plotted as black lines. Residuals to the non-linear fitting are plotted below the raw data.

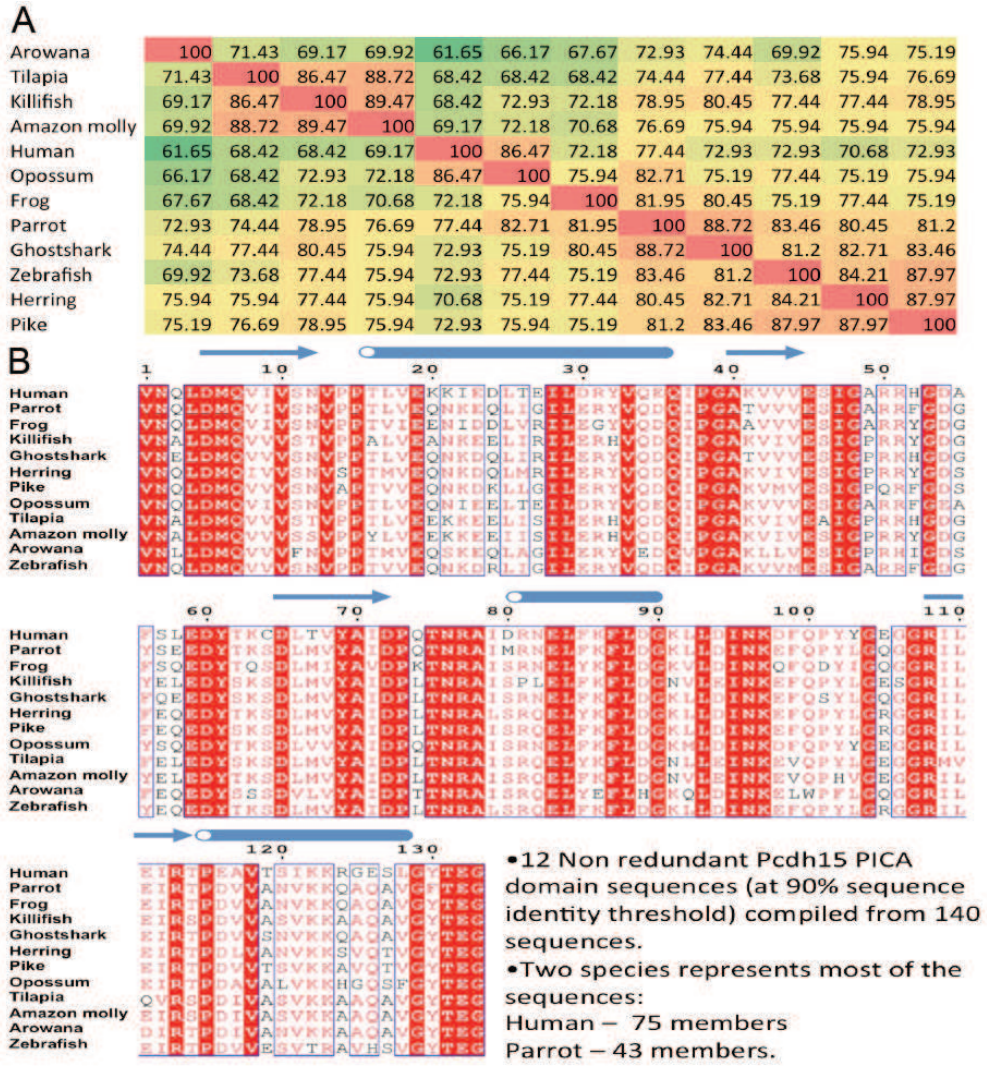

Figure S2. Conservation of the Pcdh15 PICA domain, Related to Figure 2

(A) Interspecies conservation of the PICA domain among 12 group-representative species.

(B) Sequence alignment of the PICA domains from PCDH15 from the same species. About 40% of residues are completely conserved, with almost all others conserved by chemical type. Secondary structure elements, shown in blue above the sequence alignment, are conserved across species.

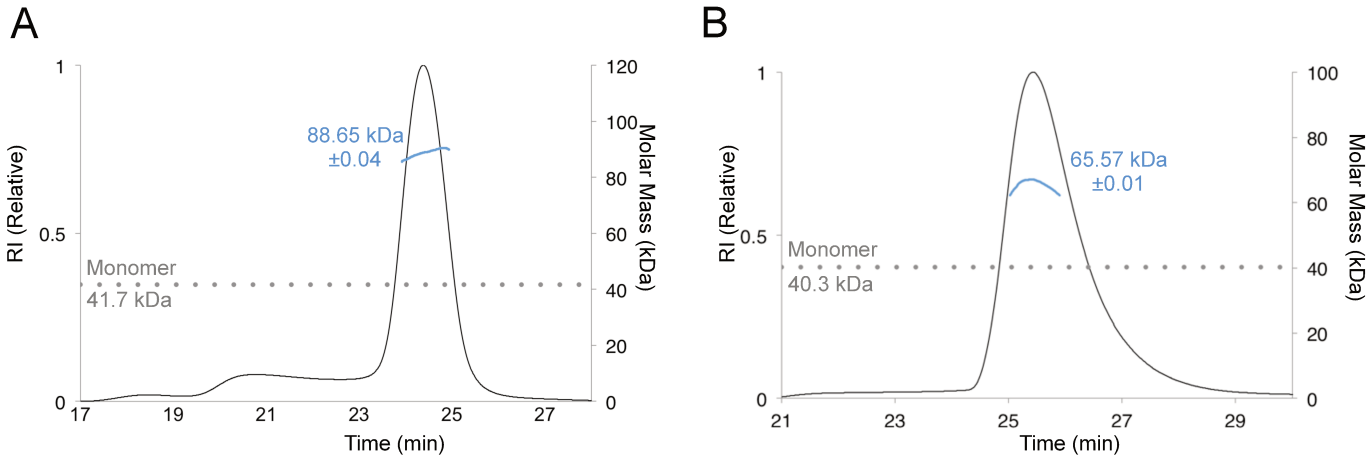

Figure S3. Evidence of Pcdh15 EC1-3 and Pcdh15 EC10-PICA Dimerization by SEC-MALS, Related to Figure 2

(A) Purified wild-type Pcdh15 EC1-3 was analyzed by size exclusion chromatography with in-line multi-angle light scattering (SEC-MALS). Refractive index changes (RI, relative) from the protein of interest is plotted in black. Molecular mass, calculated from light scattering analysis, is plotted in blue and labeled with the fitted value. The theoretical molecular mass (by sequence) is plotted as a horizontal dotted-line in grey and accompanied by a label.

(B) Purified wild-type Pcdh15 EC10-PICA analyzed by SEC-MALS.

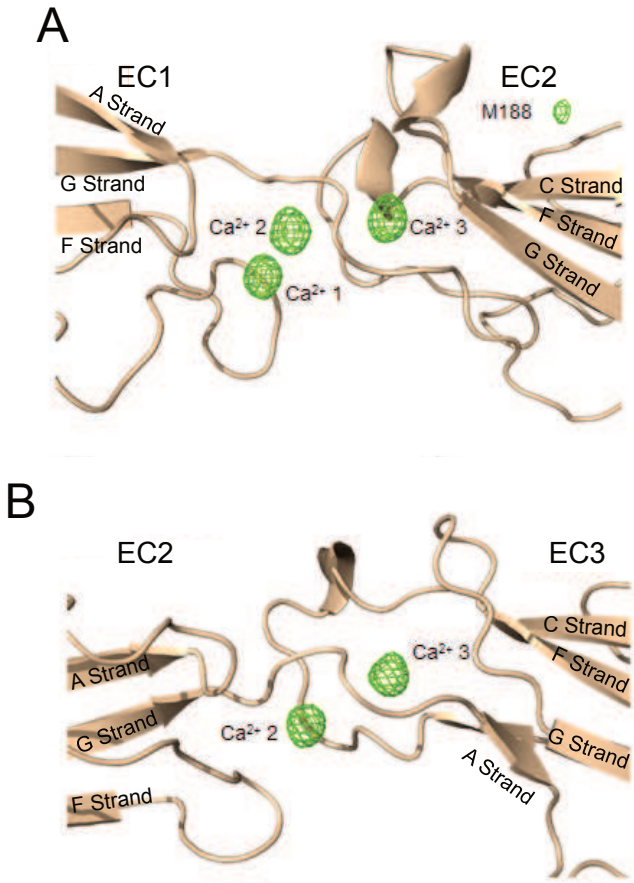

Figure S4. Non-canonical Ca^{2+} Interactions Observed Through Ca2+ Bijvoet Difference Analysis, Related to Figure 3

(A and B) Ca^{2+} anomalous difference electron density for the EC1-EC2 linker (A) and the EC2-EC3 linker (B). The EC2-EC3 linker region, which helps mediate the cis dimer, binds only two Ca^{2+} ions, rather than the canonical three.

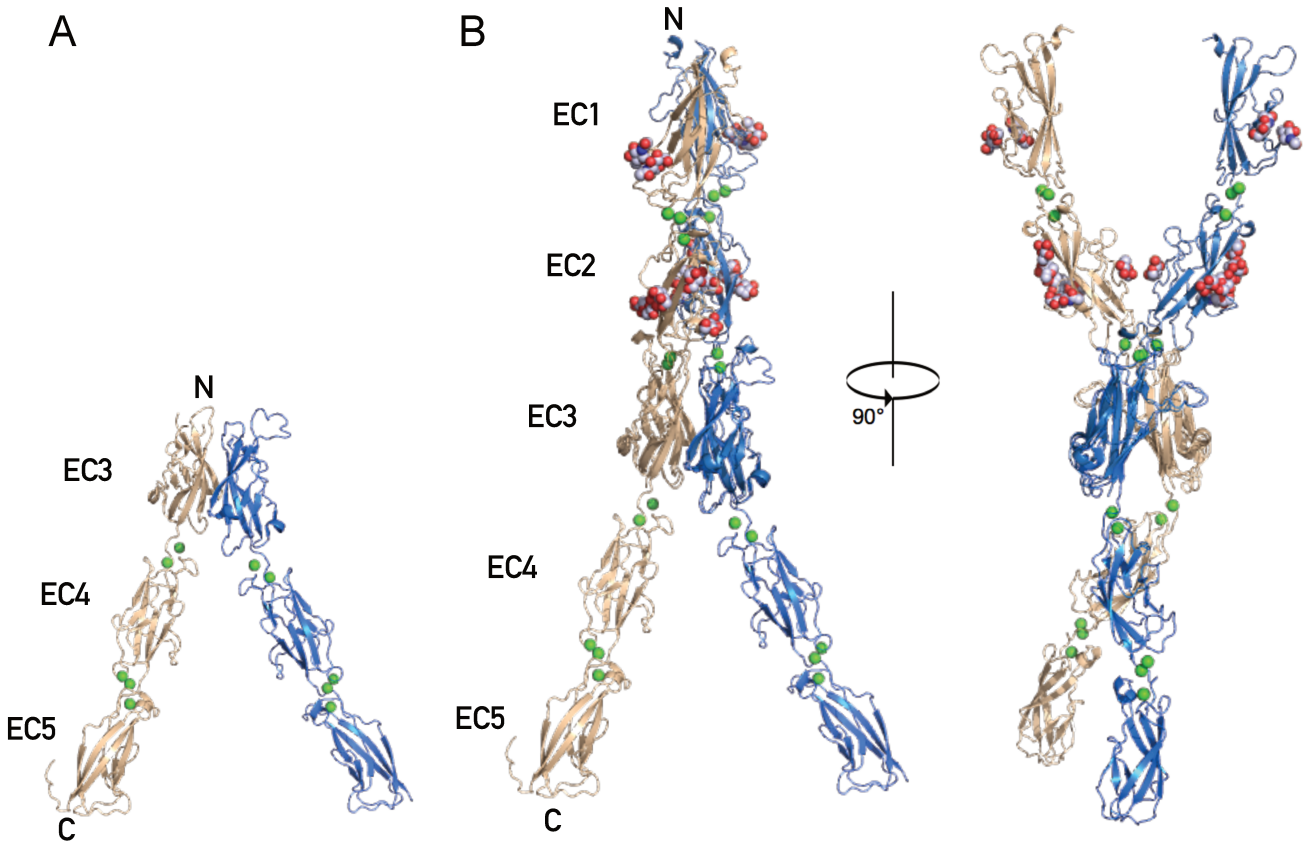

Figure S5. *Cis* Assemblies of Pcdh15 in Pcdh15 Crystal Structures, Related to Figure 3

(A) *Cis* dimer of Pcdh15 observed in Pcdh15 EC3-5, generated by application of crystallographic symmetry. (PDB ID: 5T4M)

(B) *Cis* dimer of Pcdh15 from Pcdh15 EC1-3 aligned to Pcdh15 EC3-5, RMSD= 1.73 Å.

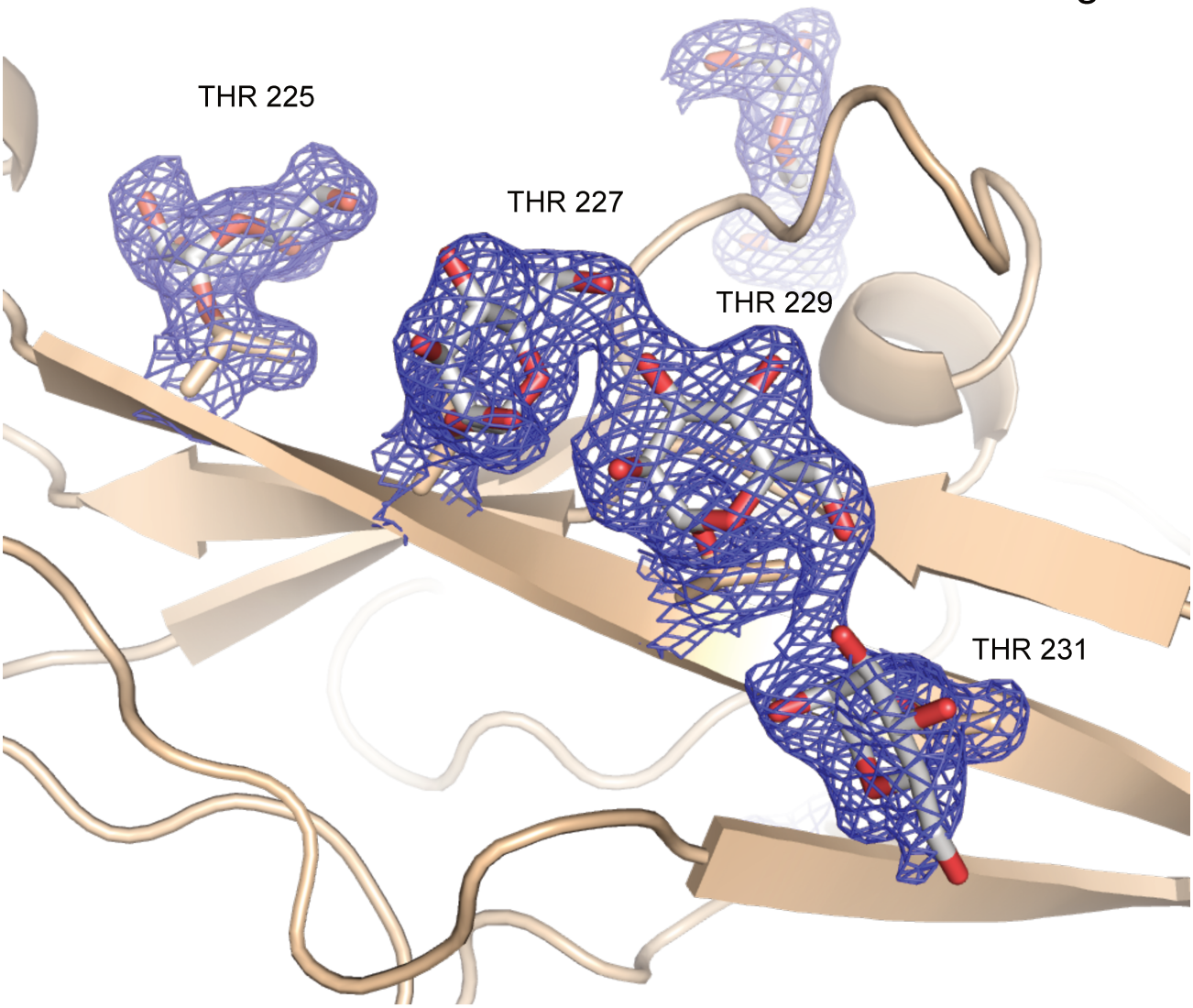

Figure S6. Electron Density for o-Mannose Moieties of Pcdh15 EC1-3, Related to Figure 3
Electron density from an F(o)-F(c) density map contoured at a σ level of 1 shown in blue mesh

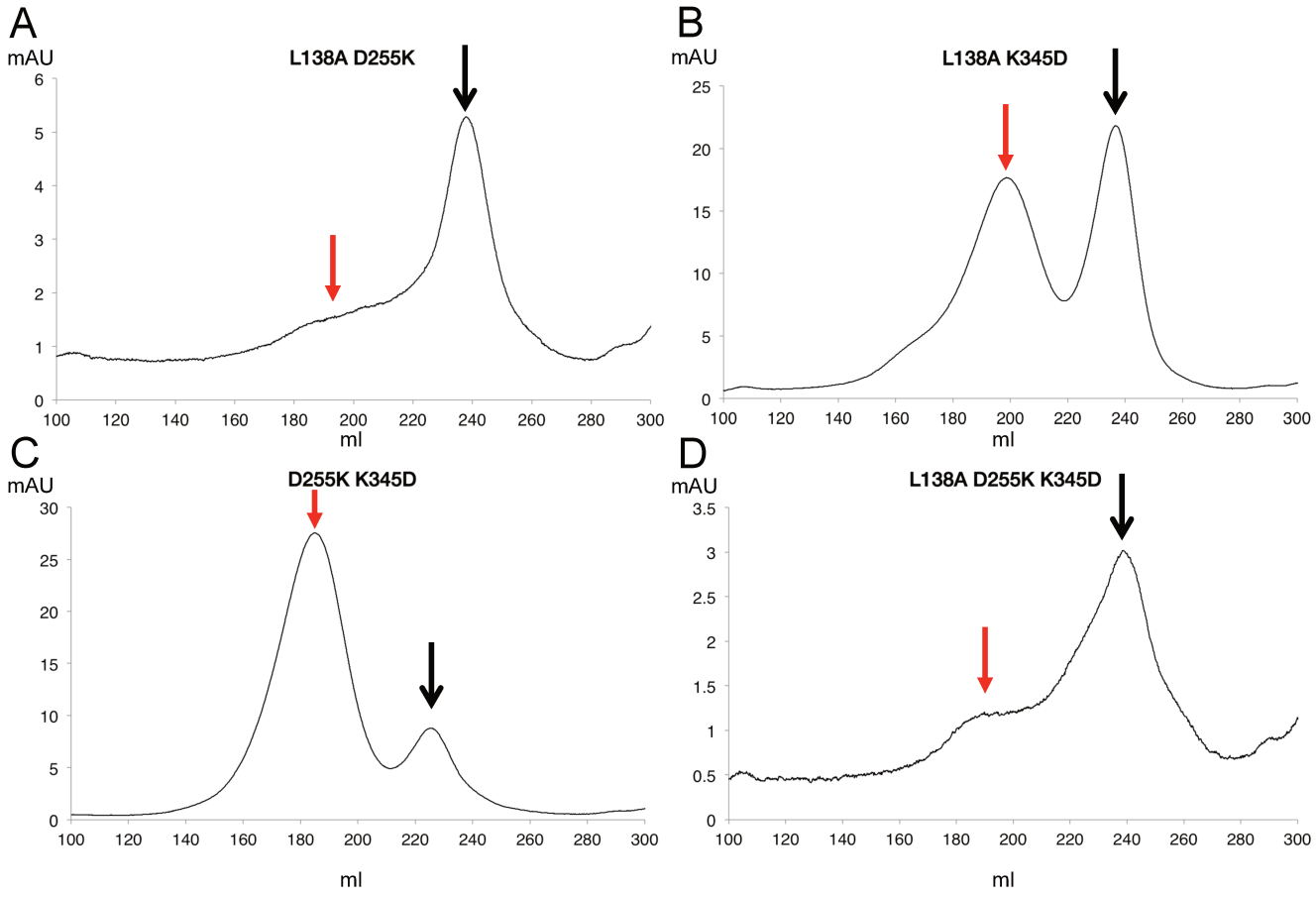

Figure S7. Size Exclusion Chromatography Traces of Pcdh15 EC1-3 Double and Triple Mutants, Related to Figure 5
(A-D) Chromatograms of Pcdh15 EC1-3 (A) L138A D255K, (B) L138A K345D, (C) D255K K345D, and (D) L138A D255K K345D . Red arrows demark dimer peaks or shoulders. Black arrows demark monomer peaks.

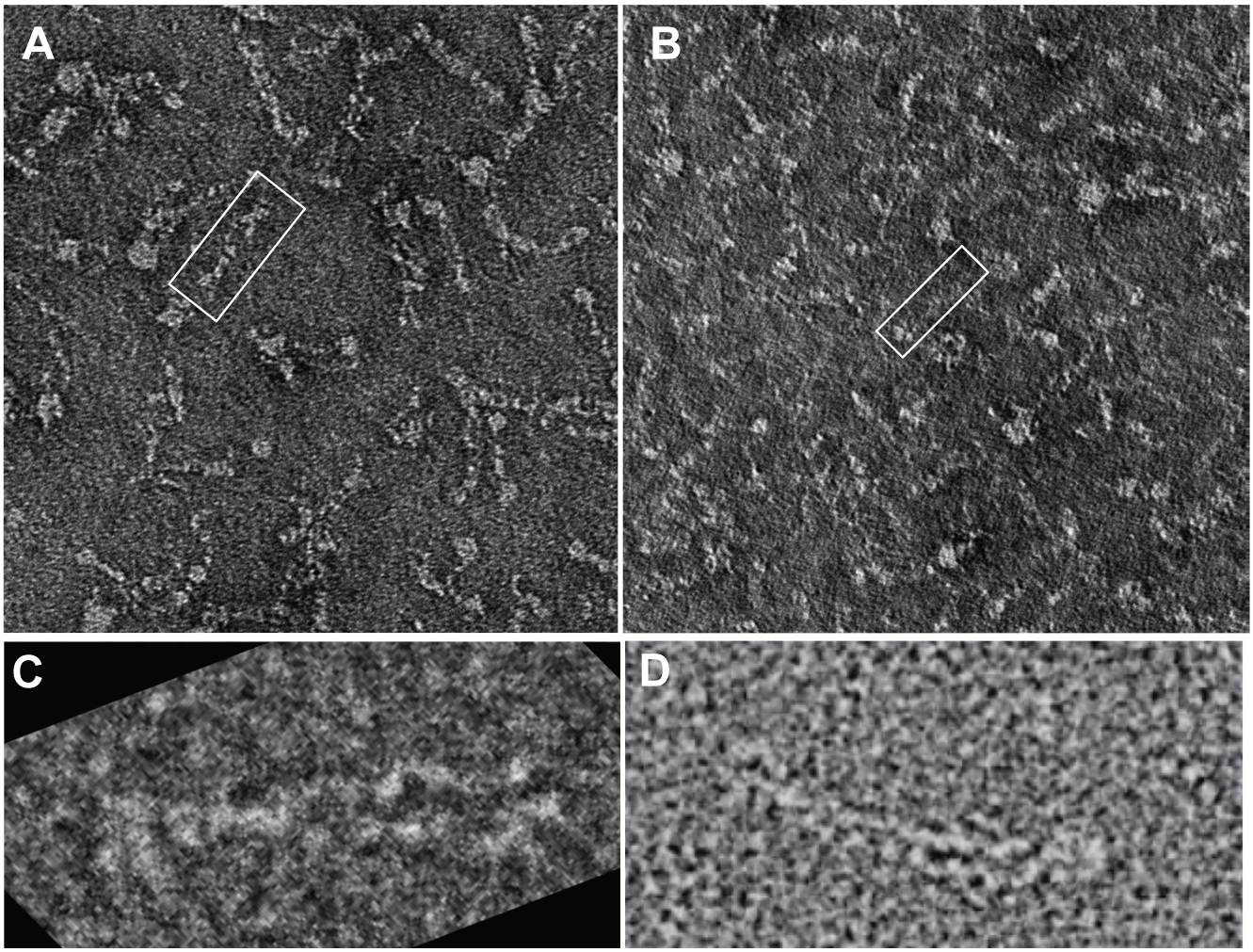

Figure S8. Negative Stain Transmission Electron Micrographs of Pcdh15 EC1-11, Related to Figure 6

(A) Electron Micrograph of Pcdh15 EC1-11 WT with a dimer singled out in the white box.
(B) Electron Micrograph Pcdh15 EC1-11 V250D with a monomer singled out in the white box.
(C and D) A comparison of negative stain transmission electron micrographs from (C) our sample and (D) the micrographs reported in Kazmeirczak et al. 2007. Image in (C) has been rotated and cropped to match the orientation in (D).